Cellular Internalization and Inhibition Capacity of New Anti-Glioma Peptide Conjugates: Physicochemical Characterization and Evaluation on Various Monolayer- and 3D-Spheroid-Based *in Vitro* Platforms

Zsuzsa Baranyai, Beáta Biri-Kovács, Martin Krátký, Bálint Szeder, Márta L. Debreczeni, Johanna Budai, Bence Kovács, Lilla Horváth, Edit Pári, Zsuzsanna Németh, László Cervenak, Ferenc Zsila, Előd Méhes, Éva Kiss, Jarmila Vinšová, and Szilvia Bősze*
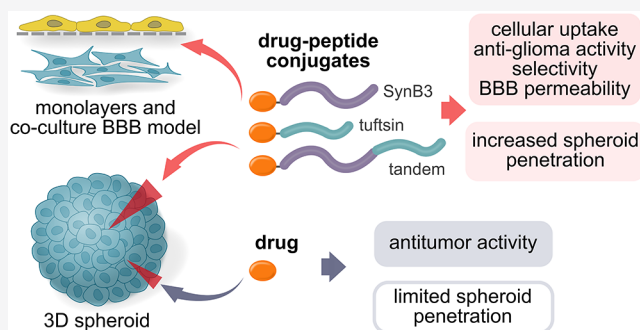
Read Online

ACCESS | Metrics & More | Article Recommendations | SI Supporting Information

ABSTRACT: Most therapeutic agents used for treating brain malignancies face hindered transport through the blood−brain barrier (BBB) and poor tissue penetration. To overcome these problems, we developed peptide conjugates of conventional and experimental anticancer agents. SynB3 cell-penetrating peptide derivatives were applied that can cross the BBB. Tuftsin derivatives were used to target the neuropilin-1 transport system for selectivity and better tumor penetration. Moreover, SynB3-tuftsin tandem compounds were synthesized to combine the beneficial properties of these peptides. Most of the conjugates showed high and selective efficacy against glioblastoma cells. SynB3 and tandem derivatives demonstrated superior cellular internalization. The penetration profile of the conjugates was determined on a lipid monolayer and Transwell co-culture system with noncontact HUVEC-U87 monolayers as simple *ex vivo* and *in vitro* BBB models. Importantly, in 3D spheroids, daunomycin-peptide conjugates possessed a better tumor penetration ability than daunomycin. These conjugates are promising tools for the delivery systems with tunable features.

INTRODUCTION

Gliomas are the most common type of primary brain tumors, accounting for 30% of all brain tumors. Gliomas are thought to originate from the neuroglial stem or progenitor cells.[1] Among the many subtypes, glioblastoma (GBM) is the most aggressive form characterized by poor prognosis and high recurrence rate. Despite the combined treatment of surgery, chemotherapy (mainly with temozolomide), and radiotherapy, the median overall survival is less than 2 years.[2−5] A glioma stem cell (GSC) subpopulation has been identified in glioblastoma, and presumably, these cells are responsible for the resistance to conventional treatments as well as for the high recurrence rate. GSCs are capable of self-renewal and differentiation, and they have high tumorigenicity.[6] Thus, more effective approaches for the treatment of gliomas and GBM are urgently needed.

The blood−brain barrier (BBB), a complex neurovascular unit, represents another difficulty in the chemotherapy of gliomas because it prevents therapeutic agents from passing through the endothelium of its capillaries and, therefore, inhibits the delivery of drugs to tumors of the central nervous system (CNS).[7,8] However, the functioning and organization of the BBB can be altered under pathological conditions. Glioblasto-

mas are characterized by various degrees of blood−brain tumor barrier (BBTB) integrity depending on the different tissue regions. In bulky tumor areas, the BBTB integrity is compromised. It can be slightly leaky in more invasive peripheral regions, while in sparsely invaded sectors distant from the tumor bulk it can be intact. Where the BBTB is compromised, the tumor could be more available for drugs; however, the intact BBTB protects regions with isolated tumor cells that can give rise to tumor recurrence.[8,9] Current noninvasive strategies to overcome the BBB exploit receptor- and adsorptive-mediated transport systems using carrier molecules and nanotechnology-based drug delivery.[8,10−12]

Cell-penetrating peptides (CPPs) are promising tools to achieve enhanced drug delivery for antitumor treatment. These

are short (usually less than 30 amino acids), positively charged peptides with amphipathic characteristics, and they are capable of rapidly entering cells without cytolytic effects.[13,14] The cationic SynB peptides (e.g., SynB1 and SynB3) belong to the CPP family and are able to cross the cellular membranes of the BBB with high efficiency.[15,16] They are derived from a natural antimicrobial peptide called protegrin-1 (PG1, RGGRLCYC-RRRFCVCVGR-NH$_2$).[17] PG1 forms an antiparallel β-sheet, constrained by two disulfide bridges. Eight PG1 peptides aggregate to form a membrane-spanning pore causing cell lysis.[18,19] Replacement of the four cysteines with serines leads to linear peptides (SynB1, RGGRLSYSRRRFSTSTGR-NH$_2$; SynB3, RRLSYSRRRF-NH$_2$, a truncated derivative of SynB1) which are able to cross cell membranes efficiently without any cytolytic effect.[15,16] The transport mechanism of these peptides has been identified as temperature- and energy-dependent adsorptive-mediated transcytosis,[16,20,21] which provides the possibility of uptake of cationic molecules at the luminal surface of endothelial cells and then the possibility of exocytosis at the abluminal side.[22] However, it is suggested by *in vitro* studies that SynB peptides are sequestered within endocytotic vesicles and might be degraded within lysosomal compartments.[21]

Different drugs with poor brain-penetrating ability (such as doxorubicin,[15,16,23] paclitaxel,[24] benzylpenicillin,[25] dalargin,[26] and morphine-6-glucuronide[27]) were conjugated to peptides from the SynB family. The conjugates, in particular, SynB3 conjugates in an *in situ* brain perfusion method, have shown an increased uptake without compromising the tight junction integrity of the BBB.[28] Antitumor drug-SynB conjugates (doxorubicin-SynB1,[23] 2-pyrrolinodoxorubicin-SynB3,[29] and paclitaxel-SynB3[24]) were able to overcome multidrug resistance *in vitro*; this finding might be explained by the fact that the conjugated drug is not recognized by the P-glycoprotein efflux pump. Increased *in vivo* BBB penetration and increased analgesic activity of SynB3-conjugated endomorphin-1 were achieved.[30] Studies on fluorescently labeled gelatin-siloxane nanoparticles conjugated to SynB1 also showed increased *in vitro* transport through the BBB and *in vivo* delivery to the brain.[31] The BBB transport characteristics (influx and efflux) of five structurally different CPPs (pVEC, SynB3, Tat 47−57, transportan 10 (TP10), TP10-2) were investigated *in vivo* (intravenous injection into mice) using radiolabeled peptides.[32] Cationic CPPs like SynB3 showed high brain influx rates, and except for pVEC, all investigated peptides demonstrated a significant efflux from the brain; however, among them, SynB3 had the lowest extent of efflux. According to this study, the estimated cell-penetrating ability of SynB3 is lower than that of pVEC;[32] therefore, despite the higher efflux rate of SynB3, a higher degree of selectivity could be achieved by its application.

CPPs provide an effective way of intracellular drug delivery; however, lack of cell-type specificity remains a major disadvantage for their clinical development. A promising strategy to increase the specificity of CPP-based drug delivery toward tumor cells is the conjugation of CPPs to targeting ligands such as homing peptides or tumor-penetrating peptides.[13] A potential target for achieving the specificity is the neuropilin-1 (NRP-1) transport system. NRP-1 is expressed in most tissues; however, it is upregulated in angiogenic tumor blood vessels (including brain endothelial cells) and usually in tumor cells.[33,34] Furthermore, it was reported that NRP-1 is overexpressed in gliomas and NRP-1 expression is increased with the elevation of glioma grade.[35] NRP-1 is a transmembrane glycoprotein with multiple domains. It functions as a coreceptor

for several extracellular ligands including various forms of vascular endothelial growth factor (VEGF) and class 3 semaphorins.[33] Among others, NRP-1 plays a crucial role in angiogenesis, axonal guidance, and cell migration.[36] The ligands of NRP-1 often possess a CendR motif (R/KXXR/K, C-end rule), which was identified as a key aspect for tumor and tissue penetration through the activation of an endocytotic/exocytotic transport named the CendR pathway.[37−40] The C-terminal lysine or arginine is crucial for the activity of the ligands. Blocking the free carboxyl group of this lysine or arginine residue by amidation or elongating the sequence with other amino acids can eliminate the binding and the cellular uptake of the peptide. However, the internal (cryptic) R/KXXR/K motif in the ligand can also be adequate, since it can be exposed and switched on by proteolytic cleavage at the site of action.[37] The binding of the cargo carrying CendR peptide to NRP-1 initiates an endocytic process that is distinct from the known endocytosis pathways.[41] This process is presumably followed by the releasing of exosomes containing CendR peptide-conjugated cargo to accomplish cell-to-cell transport and consequently effective tissue penetration (or reaching the tumor side of the endothelium).[33,40] Successful *in vitro* and *in vivo* tumor penetration of drugs or drug-loaded nanoparticles was achieved with the aid of various CendR peptides.[33,39,40]

Tuftsin is a naturally occurring tetrapeptide (human, TKPR; canine, TKPK) produced by enzymatic cleavage of the Fc domain of the heavy chain of immunoglobulin G (IgG). Tuftsin has a wide range of biological activities such as the immunostimulatory effect and antitumor activity through the activation of immunologic effector cells.[42] Furthermore, tuftsin binds to NRP-1, it has a highly similar sequence to the C-terminus of VEGF-A165 (DKPRR), and tuftsin competes with it for binding to NRP-1.[43,44] An antagonist analogue of tuftsin, TKPPR, that has a higher affinity for tuftsin receptors on phagocytic cells[45] and possesses a CendR motif, binds to NRP-1 approximately 20-fold more avidly than tuftsin.[43] Moreover, sequential oligopeptides based on tuftsin have been developed and used as effective carriers in monocyte related targeting.[46−50]

Finding new drugs is also a promising tool in the combat against gliomas. Salicylanilides (2-hydroxy-N-phenylbenza-mides) have shown a wide variety of interesting biological activities including antimicrobial and antitumor effects.[51,52] Niclosamide is an oral antihelminthic salicylanilide drug, and recent studies identified it as a potential anticancer agent. However, its poor bioavailability because of its limited water solubility is an obstacle. Niclosamide targets mitochondria by uncoupling oxidative phosphorylation and inducing cell cycle arrest, growth inhibition, and apoptosis. In addition, it also inhibits several signaling pathways (e.g., Wnt/β-catenin, mTORC1, STAT3, NF-κB, Notch).[52,53] Since the dysfunction of most of these pathways is involved in cancer stem cells, niclosamide is promising at destroying them.[54] Furthermore, the inhibitory effects of niclosamide on primary human glioblastoma cells were also demonstrated by suppressing signaling pathways. Pre-exposure to niclosamide significantly diminished the malignant potential of glioblastoma cells *in vivo*.[55] Another study found that niclosamide induced cytotoxicity in human glioblastoma cells (U87) with increased protein ubiquitination, endoplasmic reticulum (ER) stress, and autophagy.[56] Overall, these findings suggest that salicylanilide derivatives with an effective drug delivery system could be useful therapeutic candidates against GBM.

Scheme 1. Structures of (A) Salicylanilide Derivatives, (B) Daunomycin, and (C) Synthesis of Temozolomide-Carboxylic Acid, (D) Conjugation of Salicylanilide and Daunomycin to (Aminooxy)acetylated Peptide Derivatives to Obtain Drug-Peptide Conjugates with an Oxime Bond, (E) Synthesis of Temozolomide Conjugates to Obtain a Drug-Peptide Conjugate with an Amide Bond, and (F) the Summarized Schematic Structure of the Carrier Peptide Derivatives
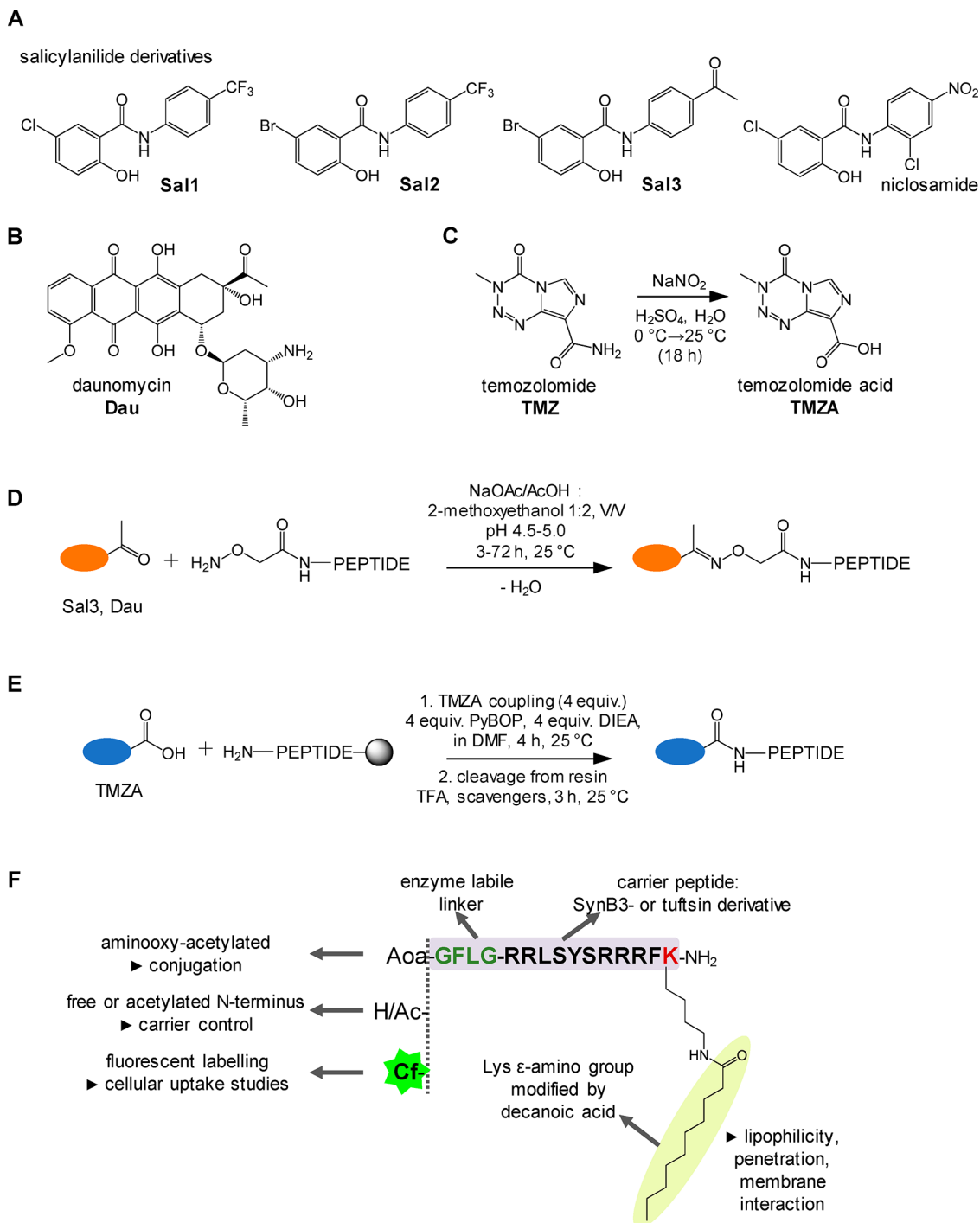
In this study, we designed drug-peptide conjugates of SynB3 and tuftsin derivatives. Conjugates of tandem peptides composed of both SynB3 and tuftsin derivatives were also used to combine the advantages of these peptides and to develop selective delivery systems. In the case of tandem peptides, we hypothesized that SynB3 derivatives used as cell-penetrating peptides with the ability to cross the BBB are more effective in transferring drugs through the endothelial barrier, whereas tuftsin derivatives as CendR peptides also assist in vascular translocation and they provide target specificity and tumor penetration.[57−61] As drug candidates against glioblastoma, we used new salicylanilide derivatives (Sal). A conventional antitumor agent daunomycin (Dau, which has a poor penetration into the brain due to the multidrug resistance mechanism[15]) and the first-line anti-glioblastoma agent temozolomide (TMZ, which is able to cross the BBB, but improved selectivity is needed[62]) were also applied. Here we report the design, *de novo* synthesis, chemical characterization,

and *in vitro* evaluation of new salicylanilide derivatives, salicylanilide-, daunomycin-, and temozolomide-peptide conjugates. Secondary structure analysis, lysosomal degradation, cytostatic and cytotoxic activity, cellular uptake, intracellular localization in cell culture monolayers, and penetration ability of conjugates on *ex vivo* and *in vitro* BBB models and into three-dimensional (3D) tumor spheroids are presented.

■ RESULTS AND DISCUSSION

Synthesis and Chemical Characterization of Peptide Conjugates. The summarized schematic structures of the compounds used in this study are presented in Scheme 1. Salicylanilide derivatives Sal1, Sal2, and Sal3 were prepared as described before.[50,63]

The carrier peptides were synthesized by solid phase peptide synthesis using the standard Fmoc/*t*Bu strategy. The synthesis of tuftsin derivatives is presented in our previous work.[50] SynB3 and tuftsin derivatives were modified with decanoic acid chains to enhance the lipophilicity, membrane affinity, cell penetration, and endosomal escape properties as well as the encapsulation efficacy of peptides.[50,64−66] Peptides with an acetylated or free N-terminus were prepared as controls. Fluorescently labeled peptides with 5(6)-carboxyfluorescein at the N-termini (Cf-peptide derivatives) were prepared for the cellular uptake studies. For the conjugation, the N-termini of the peptides were (aminooxy)acetylated (Aoa-derivatives). The C-terminus of the peptides was obtained in amide form; only in the case of TKPPR and SynB3-TKPPR, the C-terminus was obtained in carboxyl form after cleavage from resin.

Conjugable salicylanilide Sal3 (*N*-(4-acetylphenyl)-5-bromo-2-hydroxybenzamide) and daunomycin (Dau) were conjugated to the peptides via an oxime bond, directly or by the insertion of an enzyme cleavable linker (Scheme 1). The oxime bond is stable between pH 3 and 8;[67] the incorporation of a GFLG tetrapeptide between the drug and the carrier moiety might be necessary for sufficient drug release and efficacy. The GFLG linker can be cleaved by the lysosomal cathepsin B that is present at elevated levels in cancer cells.[68,69] The salicylanilide- and daunomycin-peptide conjugates were prepared by oxime bond formation from the appropriate (aminooxy)acetylated peptide and the oxo-group-containing drug molecules as described earlier.[50] The conjugation was followed by analytical RP-HPLC (Figure S1). Although doxorubicin-SynB3 conjugate (an analogue to Dau-SynB3 conjugate) was prepared and evaluated by Rousselle et al.,[16] the Dau-Aoa-SynB3 conjugate presented here represents a new molecule that is basically different from the doxorubicin-SynB3 not only in the drug molecule (Dau vs doxorubicin) but also in the bond between the drug and peptide (oxime vs amide).

The detected metabolites containing the N-terminal amino acid and drug molecule as the smallest lysosomal degradation products were also synthesized using amino acids functionalized with an (aminooxy)acetyl group, and these Aoa-amino acid derivatives were conjugated to Sal3 or Dau as described earlier.[50]

Temozolomide was modified by diazotation and hydrolysis to obtain temozolomide-carboxylic acid (TMZA) (Figures S2 and S3—characterization of TMZA). TMZA was coupled to SynB3 peptide derivatives via an amide bond on the solid phase, and the conjugates were cleaved from the resin[70,71] (Scheme 1).

The peptide derivatives and conjugates were purified using semipreparative RP-HPLC and chemically characterized by mass spectrometry (a mass coinciding with the calculated value)

and analytical RP-HPLC (a purity of at least 95%) (Table S1, Figure S4).

The compounds were characterized by their estimated lipophilicity profile by means of their retention time obtained by RP-HPLC and calculated logP values obtained by the Chemicalize online platform (https://chemicalize.com/app/calculation, ChemAxonPASS), as detailed in the Supporting Information, Figure S5. The carrier peptides are less lipophilic than the corresponding conjugates, there is no significant difference between the lipophilicity of the corresponding Dau- and Cf-peptides, while the corresponding Sal3-conjugates possess the most lipophilic character.

The stability of the conjugates was investigated under the conditions applied in *in vitro* studies using analytical RP-HPLC and mass spectrometry. The conjugates were stable in DMSO at 4 °C at least for 4 weeks. Dau-conjugates and Sal3-conjugates were stable in DMEM supplemented with 2.5% FBS (37 °C, 5% CO_2) at least for 24 h (Figure S6). The TMZ-conjugates, TMZ-SynB3 and TMZ-GFLG-SynB3, decomposed in DMEM supplemented with 2.5% FBS with a half-life of 20 min (Figure S7). TMZ is a prodrug; it is stable at acidic pH (e.g., in the stomach) but hydrolyzes at physiological pH (pH 7.4, e.g., blood, cell culture medium) to the active and unstable 5-(3-methyl-triazen-1-yl)imidazole-4-carboxamide (MTIC) which rapidly decomposes to form the highly reactive methylating agent methyldiazonium cation and to the inactive 5-amino-1*H*-imidazole-4-carboxamide (AIC).[70] Conjugated TMZ possesses the same feature in the cell culture medium, resulting in some inactive AIC-peptide derivatives.

Circular Dichroism Spectroscopic Evaluation of the Secondary Structure of SynB3 and Tuftsin Derivatives. The solution conformation of the acetylated tuftsin-antagonist peptide TKPPR, SynB3, and its tandem TKPPR derivative was studied under different solvent conditions employing CD spectroscopy in the far ultraviolet region. This highly sensitive method is widely used for determining and monitoring the secondary structure of proteins and peptides.[72] The CD curve of all acetylated peptides measured in water displayed a sole negative band with a minimum between 196 and 204 nm, suggesting the ensemble of various conformers (Figure 1A). This picture is in line with the cationic nature of SynB peptides where electrostatic repulsions between abundant, positively charged side chains hinder helix formation. The 6 nm red shift in the CD extremum of Ac-TKPPR with respect to the SynB3 spectrum is due to the different excitation energies of imino- and amino acid-containing peptide bonds. Distinct from other residues, proline is an imino acid and makes not a secondary but a tertiary amide bond, the $\pi−\pi*$ transition of which is at longer wavelengths.[73] Due to this reason, the proline residues also affect the λ_{min} position of the tandem peptide, shifting it to 199 nm (Figure 1A). However, in a helix-promoting solvent like trifluoroethanol (TFE), this coil-like CD feature changed considerably to an intense, $\pi−\pi*$ type CD couplet and an unresolved broad $n−\pi*$ component centered around 220 nm (Figure 1B,C). This spectral pattern is indicative of the TFE-induced formation of an organized, right-handed α-helical secondary structure.[74] Since haloalcohols provide a membrane-mimicking environment,[75] these spectroscopic results predict that upon contact with lipid membranes Ac-SynB3 readily adopts amphipathic helices. Compared to the parent peptide, qualitatively similar spectral alterations were obtained for the Ac-SynB3-TKPPR derivative (Figure 1B,C). Noticeably, however, the magnitude of the positive branch of the CD
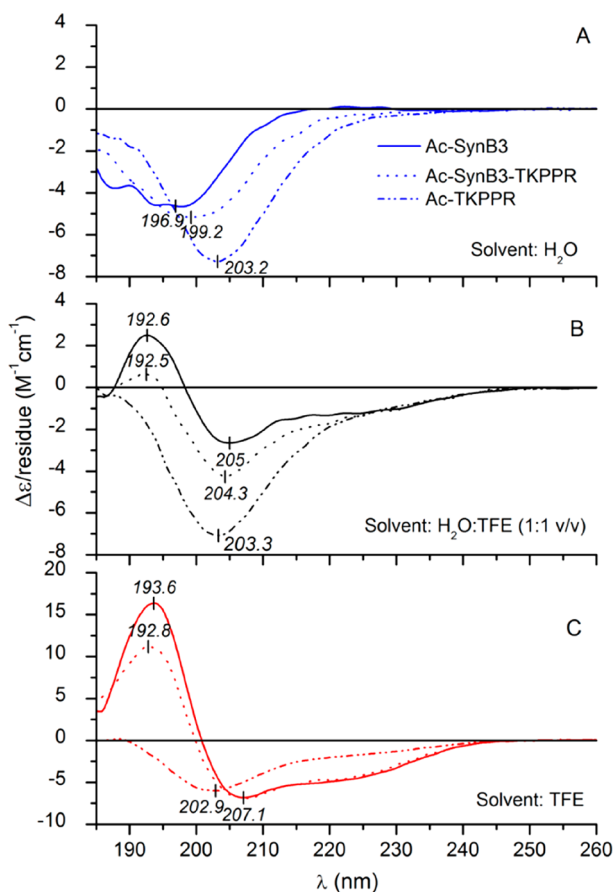
Figure 1. Far-UV CD spectra of SynB3 peptides and TKPPR measured in (A) deionized water, (B) water:TFE 1:1 mixture, and (C) 100% TFE.

Table 1. Estimation of the Secondary Structure Content (%) of Acetylated SynB3 and TKPPR Peptides[a]

peptide	H$_2$O	H$_2$O:TFE	TFE
Ac-SynB3			
α-helix	0	14	64
β-sheet	19	16	6
disordered	65	44	8
turns	16	26	22
R^2	0.9909	0.9340	0.9660
Ac-TKPPR			
α-helix	8	14	18
β-sheet	0	0	0
disordered	78	73	64
turns	14	13	18
R^2	0.9906	0.9946	0.9960
Ac-SynB3-TKPPR			
α-helix	0	10	48
β-sheet	18	28	16
disordered	72	55	26
turns	10	7	10
R^2	0.9940	0.9683	0.9780

[a]Far-UV CD spectroscopic data were analyzed by using the MS Excel version of the PEPFIT program.

couplet at 193 nm lags behind that of Ac-SynB3 in both TFE and TFE−H$_2$O mixture which refers to the less prone helical folding of the tandem peptide. This conclusion is supported by the CD curves of Ac-TKPPR that exhibited minor variations only upon the addition of TFE (Figure 1B,C). The amplitude of the main band at 203 nm reduced modestly, and a very weak positive peak developed below 190 nm together with a slight intensification of the n−π* signals above 215 nm. According to these observations, the pentapeptide is highly resistant to the helix-promoting effect of TFE that is related to the high abundance of the helix breaker proline residues.[76,77] Thus, its coupling to SynB3 does not improve but rather impairs the overall helical propensity of the hybrid sequence. It is to be noted that the experimental CD spectra of the tandem compound can be approximated as the arithmetic sums of scaled CD curves of native SynB3 and TKPPR measured in the same solvent (data not shown). Therefore, it seems that the original structural properties of the covalently linked components in the hybrid peptide are not much altered and thus display additive CD contributions.

The outcomes of the above qualitative evaluation were in general agreement with the results of the deconvolution of the CD spectra into major structural components (Table 1). The unordered fraction represents a prominent contribution (~70−80%) for each peptide dissolved in water. Upon rising TFE concentrations, it progressively declines for Ac-SynB3 and the tandem derivative but hardly reduces in Ac-TKPPR. Concomitantly, at the expense of that content, the α-helical

component greatly increased in both SynB3 peptides albeit to a lesser extent for the hybrid sequence which exhibits a significant (26%) unordered fraction even in 100% TFE.

Lysosomal Digestion Profile of the Conjugates in Rat Liver Lysosomal Homogenate. If the conjugates get into the lysosomes, they can undergo hydrolysis at the lysosomal acidic pH (pH 4.5−5.0) and in the presence of hydrolytic enzymes.[78] To identify the smallest drug-containing metabolite, we investigated the digestion profile of the conjugates in rat liver lysosomal homogenate by LC-MS. Analyses (LC-MS chromatogram, mass spectra) of the degradation process are presented in Figures S8−S14.

The detected main cleavage sites of the conjugates are summarized in Figure 2A. As was observed in previous studies,[50,79] the smallest, drug-containing metabolite is the oxime bonded drug molecule with the N-terminal amino acid of the conjugates that are listed in Figure 2B. No significant cleavage of the oxime bond and no free salicylanilide or Dau was observed. The degradation of Sal3-Aoa-SynB3 was very fast, and after 4 h, the main metabolite was the smallest one, Sal3-Aoa-Arg-OH. The degradation of Dau-Aoa-SynB3 was also quick with a similar pattern to Sal3-Aoa-SynB3. After 5 min, in both cases, the main metabolite was released by the cleavage of the -^{2}Arg-^{3}Leu- bond (Sal3-Aoa-RR-OH and Dau-Aoa-RR-OH), but interestingly in the case of Dau-Aoa-SynB3, the degradation of Dau-Aoa-RR-OH into Dau-Aoa-Arg-OH was not complete even after 24 h, as we could find both metabolites. However, it was observed that the -Arg-Leu- bond is a favorable cleavage site in all SynB3-containing conjugates. For the enzyme-labile-linker-containing conjugate, Sal3-Aoa-GFLG-SynB3, the presence of the GFLG linker led to an increased degradation rate as we observed in previous studies.[50,79] The smallest drug-containing metabolite already appeared after 5 min in a small amount, and after 1 h, only this metabolite could be detected. However, in the case of Dau-Aoa-GFLG-SynB3, Dau-Aoa-Gly-OH appeared later, after 1 h, in a small amount. The Dau-Aoa-GF-OH was the main metabolite for 8 h, and it was still present after 24 h in a small amount. In the case of Sal3-Aoa-TKPPR[50]
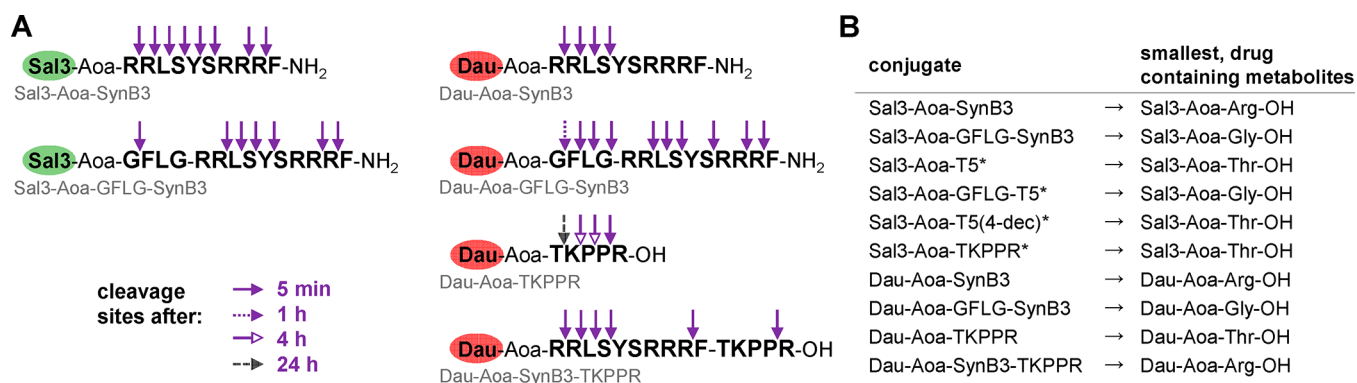
Figure 2. (A) Main cleavage sites during the degradation process of new conjugates in rat liver lysosomal homogenate and (B) the smallest, drug-containing metabolites produced from the conjugates (*: results are taken from ref 50).

and Dau-Aoa-TKPPR, the first cleavage site after 5 min was the cleavage of the -^{4}Pro-^{5}Arg- bond. The detected drug-Aoa-TKPP-OH metabolites turned out to be highly stabile in rat liver lysosomal homogenate; these were the main metabolites after 24 h in both cases. Sal3-Aoa-Thr-OH appeared after 1 h, while Dau-Aoa-Thr-OH only appeared after 24 h in a very small amount, and this might affect the cytostatic activity of both TKPPR conjugates. The Dau-Aoa-SynB3-TKPPR tandem conjugate had the same degradation pattern as Dau-Aoa-SynB3; after 24 h, the released metabolites were Dau-Aoa-RR-OH and Dau-Aoa-Arg-OH. Overall, the type of the conjugated drug also played a role in the release of the smallest, drug-containing metabolites. The resulting two amino acid-containing Dau-metabolites had a slower degradation rate than the corresponding Sal3-metabolites.

***In Vitro* Cytostatic and Cytotoxic Activity.** Determination of the *in vitro* cytostatic (inhibition of cell growth and multiplication) or cytotoxic (direct killing effect, direct decrease in cell viability) effect of the compounds was carried out on different cell cultures using MTT or SYBR-Green assay. The U87 human glioblastoma cell line is a model cell for gliomas. To compare the activity of the compounds, we also used a different brain tumor model, the MDA-MB 435Br brain metastasis cell line.[80] MDA-MB 435 was originally classified as a breast cancer cell line,[81] but recent findings point to a rather melanocytic origin of this cell line.[82] In this study, we used a subcell line of MDA-MB 435 that was established from a brain metastasis in nude mice. Human umbilical vein endothelial cells (HUVECs) were used to model tumor related vascular endothelial cells and also healthy, nontumor cells to get insight into the selectivity of the compounds. Furthermore, the MonoMac6 human monocytic cell line was used for modeling phagocytes that eliminate foreign substances such as conjugates from the blood. The HepG2 human hepatocellular carcinoma cell line represents a model to test hepatotoxicity. The cytostasis results on U87 and MDA-MB 435Br and cytotoxicity results on HUVECs of selected compounds after 24 h of treatment are presented in Figure 3 (for statistical analysis, see Figures S15 and S16). The IC$_{50}$ values corresponding to all studied compounds on the aforementioned cell cultures, completed with the 3 h cytostatic effect on U87 cells, the 3 and 24 h cytostatic effect on MonoMac6, the 24 h cytostatic effect on HepG2 cells, and the 24 h cytotoxic effect on U87 cells, are summarized in Table S2.

In the case of the U87 cells during a short, 3 h treatment, we observed that free salicylanilides had high cytostatic activity with the exception of the conjugable Sal3 (Table S2). Salicylanilides
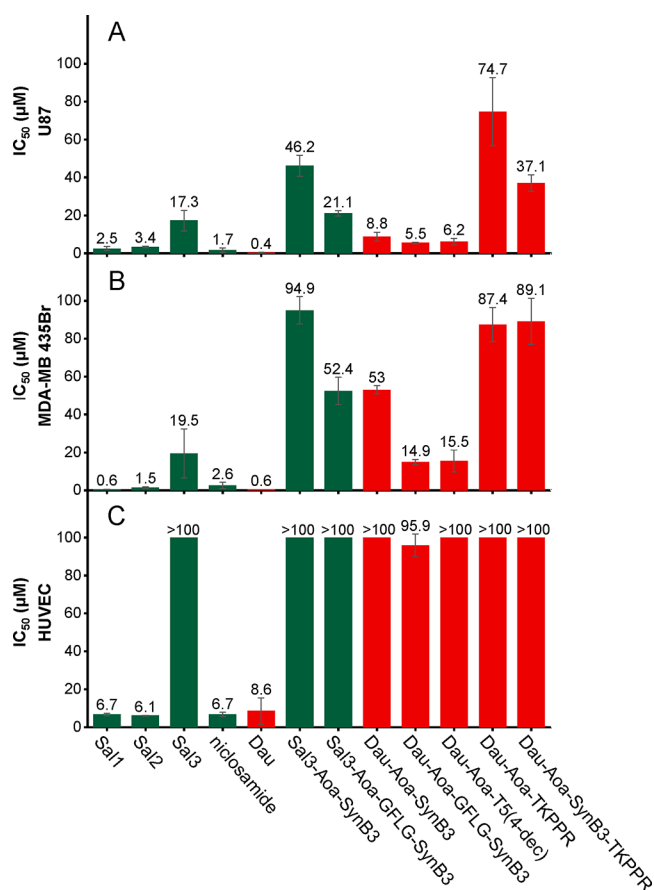
Figure 3. *In vitro* cytostatic activity of the representative compounds on (A) U87 and (B) MDA-MB 435Br cell cultures and (C) cytotoxicity on HUVEC after 24 h treatment. Experiments were carried out in duplicates; error bars represent standard deviation.

(Sal1, Sal2, niclosamide) that both in the salicylic acid ring and in the aniline ring contain halogen substituents are more potent than Sal3 where halogen on the aniline ring was replaced by an acetyl group.[50] During the longer, 24 h treatment, the IC$_{50}$ values of the salicylanilides decreased and even Sal3 had a high cytostatic activity (Figure 3). As expected, Dau had the lowest IC$_{50}$ value in the case of all of the examined cell lines. However, under these experimental circumstances, TMZ was ineffective probably due to its rapid decomposition under physiological conditions.[70] Most of the control peptides had no cytostatic activity on U87 cells, except for the SynB3 derivatives with the
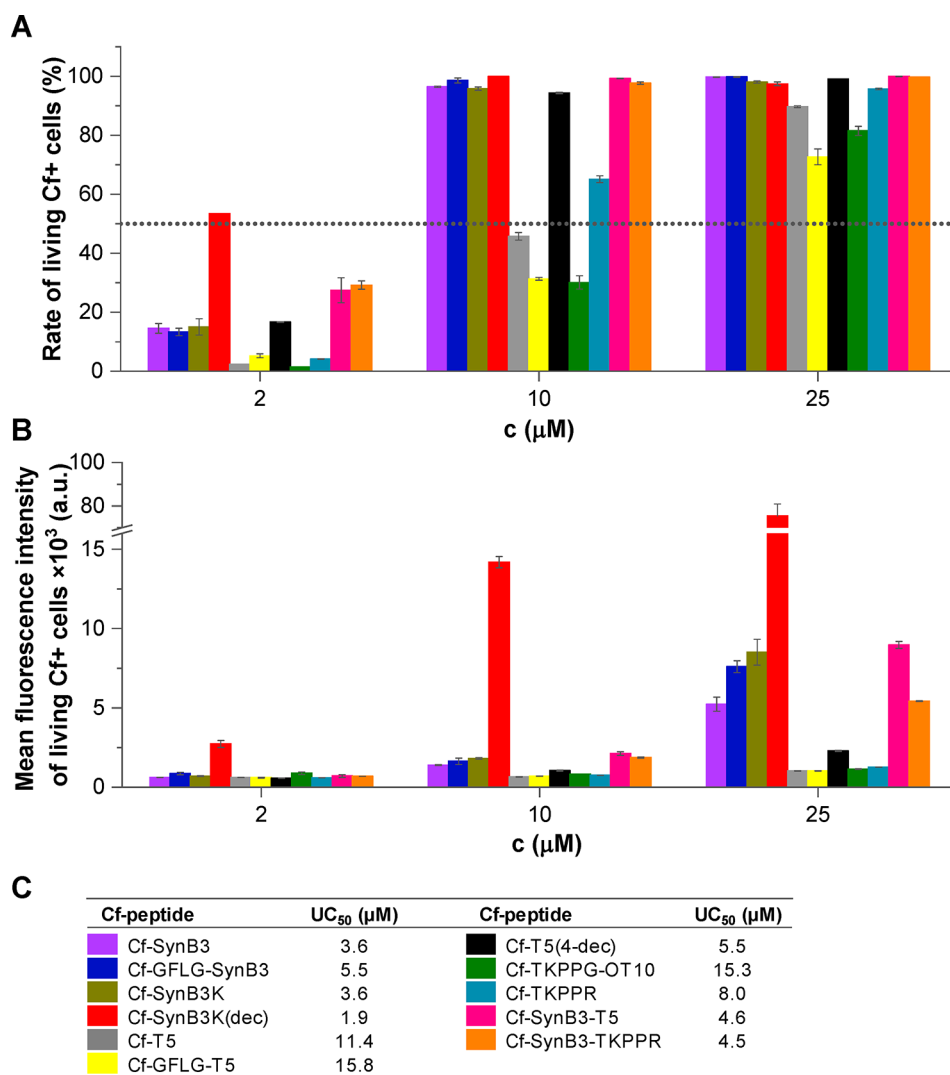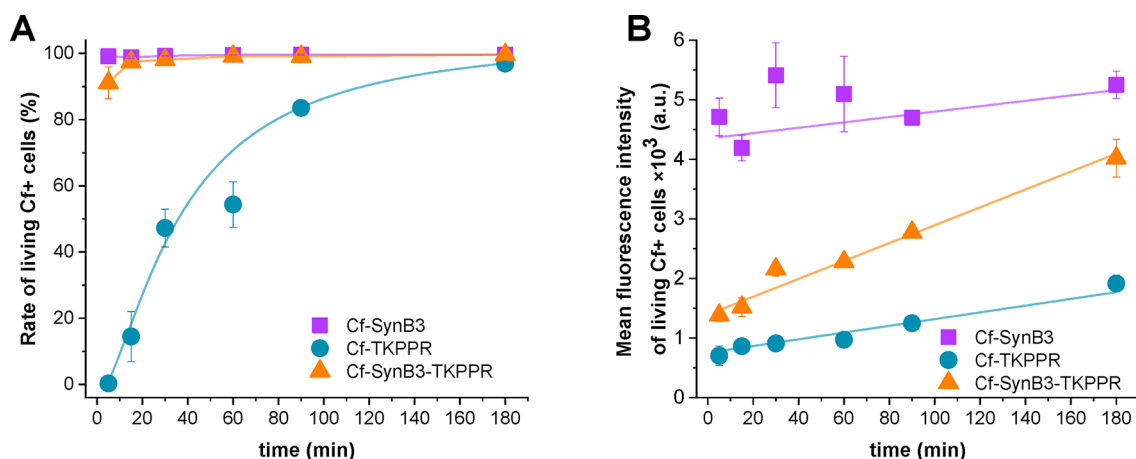
Figure 4. Comparison of the cellular uptake of the 5(6)-carboxyfluorescein-labeled peptide derivatives on U87 cells at different concentrations using flow cytometry (3 h incubation time). (A) The ratio of living, fluorescence positive cells, (B) mean intracellular fluorescence intensity of living, fluorescence positive cells, and (C) quantified value of the uptake rate (UC_{50}) of the peptides. Experiments were carried out in duplicates; error bars represent standard deviation.

decanoic acid side chain modification showing moderate cytostatic activity. These molecules containing a hydrophobic decanoyl side chain and a hydrophilic cationic peptide have an amphipathic characteristic; thus, probably they are more capable of damaging the cell membrane and causing cell death. Importantly, salicylanilide-SynB3 conjugates (Sal3-Aoa-SynB3 and Sal3-Aoa-GFLG-SynB3) had cytostatic activity after 3 h in contrast with the free Sal3. After 24 h treatment, the conjugate with the enzyme labile linker (Sal3-Aoa-GFLG-SynB3) had a similar IC_{50} value to the free Sal3 ($21.1 \pm 1.4\ \mu M$ vs $17.3 \pm 5.4\ \mu M$, respectively, Figure 3A). The Sal3-tuftsin conjugates were ineffective at the highest measured concentration with the exception of the decanoyl-containing conjugate, Sal3-Aoa-T5(4-dec), which is in correlation with the lysosomal degradation and cellular uptake of these conjugates.[50] The Dau-SynB3 conjugates showed outstanding cytostatic activity against U87 cells; however, the IC_{50} values did not decrease significantly with the longer treatment time (IC_{50} between 5.5 and 17.0 μM after 24 h). The Dau-tuftsin conjugates were also ineffective after 3 h with the exception of the decanoyl-containing conjugate, while, after 24 h, they all showed cytostatic activity mostly with similar

or slightly higher IC_{50} values (6.2−74.7 μM) than the Dau-SynB3 conjugates. The Dau-Aoa-TKPPR conjugate was the least effective among them with a moderate IC_{50} value. The tandem conjugates (Dau-Aoa-SynB3-T5, Dau-Aoa-SynB3-TKPPR) had cytostatic activity after 24 h and also after 3 h with IC_{50} values between the IC_{50} values of Dau-Aoa-SynB3 and the corresponding tuftsin conjugates (Dau-Aoa-T5, Dau-Aoa-TKPPR). The TMZ-conjugates acted similarly as the free TMZ; their rapid decomposition resulted in no cytostatic effect. The smallest metabolites of the salicylanilide conjugates produced during lysosomal degradation (Figure 2) had no activity on any of the studied cell cultures. In contrast, the metabolites of the Dau-conjugates showed cytostatic activity against U87 cells with the exception of Dau-Aoa-Thr-OH metabolite (Table S2).

The salicylanilides had outstanding activity on the MDA-MB 435Br breast tumor brain metastasis cell line, and the conjugable Sal3 also had a high cytostatic activity after 24 h treatment (IC_{50} between 0.6 and 19.5 μM, Figure 3B). The activity of the conjugates showed a similar tendency as in the case of U87 cells but with higher IC_{50} values. The most active ones were the Dau-Aoa-GFLG-SynB3 conjugate with the enzyme labile linker and

Figure 5. Time dependence of the cellular internalization of cell-penetrating peptide Cf-SynB3, tuftsin derivative Cf-TKPPR, and their tandem conjugate Cf-SynB3-TKPPR. (A) Comparison of the ratio of the living fluorescence positive U87 cells and (B) mean fluorescence intensity of living, fluorescence positive cells at different incubation times at 25 μM.

the Dau-Aoa-T5(4-dec) conjugate with the decanoyl side chain; both conjugates have amphipathic characteristics.

In the case of HUVECs, Dau and most of the salicylanilides had similar cytotoxic activity with low IC_{50} value (6.1−8.6 μM, Figure 3C). In contrast, Sal3, the control peptides, and the Sal3- and Dau-conjugates were not cytotoxic on HUVECs at the highest measured concentration; only Dau-Aoa-GFLG-SynB3 showed a slight cytotoxic effect (Figure 3C, Table S2).

Altogether, in the case of the Sal3-SynB3 conjugates and all Dau-peptide conjugates, the *in vitro* cytostatic and cytotoxic activity against U87 and MDA-MB 435Br is preserved upon conjugation to the peptides through an oxime bond, although the IC_{50} values of the conjugates in most cases are higher than the IC_{50} values of the free drugs. However, this decrease in activity could be compensated by the possible selectivity and reduction in toxic side effects provided by the conjugation.[83−85] If we compare the lack of cytotoxicity of the conjugates on HUVECs with the good cytostatic and cytotoxic activity on U87 and MDA-MB 435Br tumor cell lines, we can conclude that the conjugates have *in vitro* selectivity toward the tumor cells.

Cellular Internalization of Fluorescently Labeled Carrier Peptides. The pH dependence of the fluorescence intensity of 5(6)-carboxyfluorescein-labeled peptides and daunomycin-conjugates was studied in a pH range between 4.0 and 7.6, representing the pH values of different cellular compartments.[50,86] The results are presented in Figures S17 and S18. The fluorescence intensity of Cf-peptides showed pH dependence, while Dau-conjugates showed no significant emission changes. In both cases, the SynB3 derivatives had a slightly lower fluorescence intensity than the tuftsin derivatives and the intensities of the tandem derivatives were between the value of SynB3 and the value of tuftsin derivatives.

The *in vitro* cellular uptake of Cf-peptides was studied on the U87 cell culture using flow cytometry. The cells were treated with the compounds, and after washing and trypsinization, the rate of fluorescence positive, living cells (rate of living Cf+ cells) and the intracellular fluorescence intensity of this population (mean fluorescence intensity of living Cf+ cells) were measured and are related to the cellular uptake rate. A quantified value of the uptake rate, UC_{50} (concentration of compounds where the rate of fluorescence positive cells reaches 50%[74]) can be drawn from the ratio of fluorescence positive cells at different concentrations. Furthermore, from the rate of all living cells at

different compound concentrations, the cytotoxicity of the compounds (IC_{50} value) can be determined.

The surface-bound peptides were removed by treating the cells with trypsin for different incubation times.[87] This proteolytic step is used to detach adherent cells from the cell culture plate as well as to digest the cell surface proteins and surface-bound peptides. To detach U87 cells from the wells, in general, 3 min of trypsinization was used. Increasing the treatment time of trypsinization did not result in a significant decrease in fluorescence intensity (Figure S19A). In order to distinguish membrane-bound peptides from internalized ones, trypan blue was also used to quench the external fluorescence. Trypan blue is impermeable for living cells and quenches the extracellular green fluorescence; therefore, only the internal fluorescence can be detected.[88] No significant difference was observed after eliminating the cell-surface associated fluorescent signal (Figure S19B,C). These results obtained from longer trypsin treatments and trypan blue quenching indicate that the majority of the peptides were internalized rather than associated with the cell membrane.

The uptake of all carrier peptides on U87 cells was compared, and cells were treated with up to 50 μM concentrations of the peptides for 3 h. Their uptake was concentration dependent, as we can see in Figure 4 and with more details in Figure S20. At concentrations where nearly 100% of the cells are fluorescence positive (all cells contain fluorescent peptide, Figure 4A), we can see the differences in the corresponding mean fluorescence intensity (Figure 4B) and also in the determined UC_{50} values (Figure 4C). The SynB3 derivatives had a significantly higher uptake rate than the uptake rate in the case of the tuftsin derivatives. This finding is in line with the secondary structure of the peptides, suggesting that upon contact with lipid membranes SynB3 derivatives adopt amphipathic helices while tuftsin derivatives remain disordered. The decanoyl-containing SynB3 derivative (Cf-SynB3K(dec)) had an extremely high internalization rate, but it showed a cytotoxic effect with an IC_{50} value of 41.9 μM (Figure S20). All of the other carrier peptides showed no cytotoxicity at the highest concentration (50 μM). Among the tuftsin derivatives, the presence of the decanoyl side chain (in Cf-T5(4-dec)) also enhanced the uptake rate but without causing cytotoxicity. Using the tuftsin derivative Cf-TKPPG-OT10 with the same net charge as the cell-penetrating peptide Cf-SynB3 (the net charge at neutral pH is +5 for both) did not
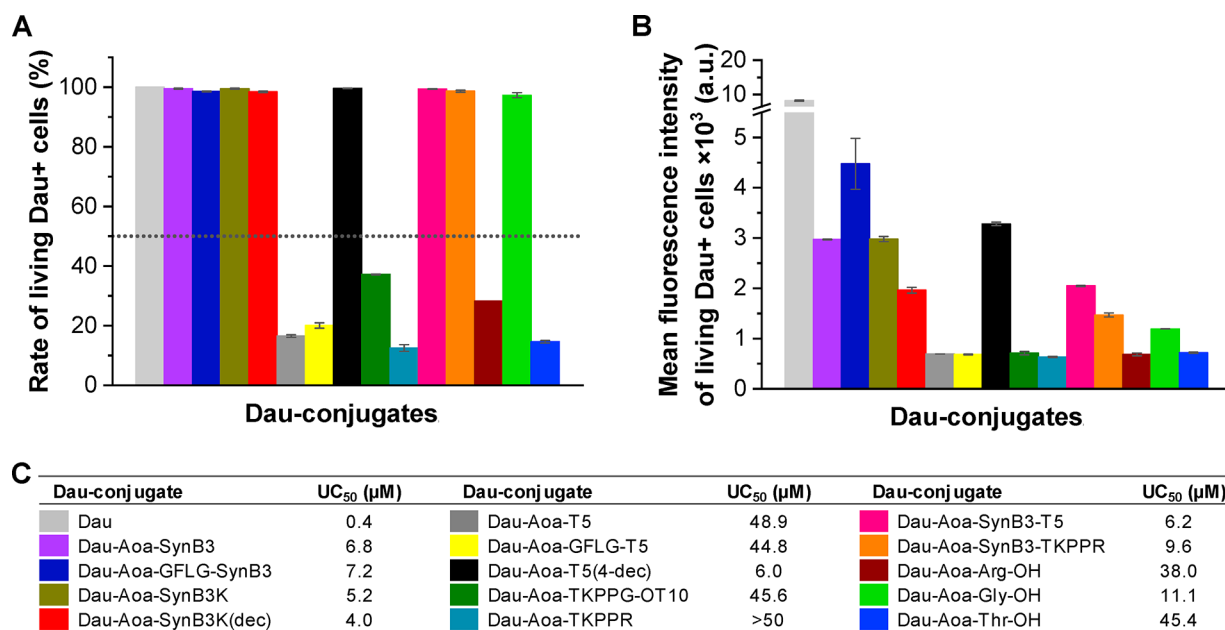
Figure 6. Comparison of the cellular uptake of Dau-peptide conjugates at 25 μM on U87 cells using flow cytometry (3 h incubation time). (A) The ratio of living, fluorescence positive cells, (B) mean intracellular fluorescence intensity of living, fluorescence positive cells, and (C) quantified value of the uptake rate (UC$_{50}$) of the conjugates. Experiments were carried out in duplicates; error bars represent standard deviation.

result in a similar internalization rate, since Cf-TKPPG-OT10 had as low of an uptake rate as most of the other tuftsin derivatives. The internalization profile of the tandem peptides (Cf-SynB3-T5, Cf-SynB3-TKPPR) was similar to Cf-SynB3. The intracellular fluorescence intensity of the cells treated with these three peptides was the highest in the case of the tandem Cf-SynB3-T5 at 25 and 50 μM. According to the performed statistical analysis (Kruskal−Wallis test with multiple comparisons), the fluorescence intensity profile of Cf-SynB3K(dec) is significantly different from the profile of peptides Cf-T5, Cf-GFLG-T5, Cf-T5(4-dec), and Cf-TKPPR (for details, see Table S3).

We also studied the time dependence of the internalization rate of the cell-penetrating peptide Cf-SynB3, tuftsin derivative Cf-TKPPR, and their tandem conjugate Cf-SynB3-TKPPR at 25 μM between 5 min and 3 h (Figure 5). In the case of Cf-SynB3, the ratio of fluorescence positive cells reached 100% very rapidly and after 5 min there was no significant increase in the mean intracellular fluorescence intensity of the cells. Rapid cellular uptake was observed also in the case of the tandem peptide in the aspect of the percentage of fluorescence positive cells; however, the intracellular fluorescence intensity further increased with time. Even after 3 h, the internalization rate of the tandem peptide remained slightly below the rate of the parent Cf-SynB3. Peptide Cf-TKPPR demonstrated slower cellular uptake it took 3 h to reach 100% of fluorescence positive cells and the corresponding fluorescence intensity is much lower than the intensity of the other two peptides.

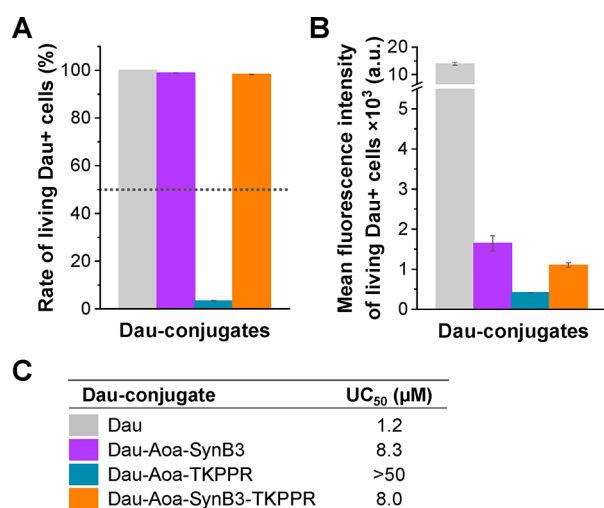**Cellular Internalization of Dau-Peptide Conjugates.** The *in vitro* cellular uptake of the Dau-peptide conjugates was also compared on the U87 cell culture using flow cytometry. The cells were treated with the compounds for 3 h, and after washing and trypsinization, the intracellular fluorescence intensity of the cells was measured. The uptake of the compounds was concentration dependent on U87 cells, as we can see in Figure S21. Results obtained at 25 μM conjugate concentration are shown in Figure 6. The internalization of the free Dau was the

highest, as expected. Interestingly, the ratio of the fluorescence positive cells after the treatment with Dau-conjugates was lower than in the case of the treatment with the corresponding Cf-peptides. The ratio of fluorescence positive cells reached nearly 100% in the case of all Cf-peptides at 50 μM concentration. However, the ratio for most of the Dau-conjugates with tuftsin derivatives is below 100% at 50 μM (Figure S21). This shows the obvious fact that labeling molecules also have a role in the internalization processes and it can cause a significant difference in the uptake of the same peptide derivative (Dau can also be considered as a labeling molecule).[89] However, mostly similar conclusions can be drawn if we compare the different conjugates to each other: the uptake rates of Dau-SynB3-conjugates were significantly higher than the uptake rates of most Dau-tuftsin-conjugates; the rate of the tandem conjugates resembled or was slightly lower than the rate of Dau-Aoa-SynB3. The SynB3-conjugates with high amphipathic characteristics showed a cytotoxic effect: hydrophobic-linker-containing Dau-Aoa-GFLG-SynB3 and hydrophobic-decanoyl-containing Dau-Aoa-SynB3K(dec) had an IC$_{50}$ value of 28.2 and 32.0 μM, respectively (Figure S21). The uptake of Dau-Aoa-SynB3K-(dec) was not outstanding compared to the uptake of its Cf-analogue (Cf-SynB3K(dec)). Interestingly, the uptake of the decanoyl-containing tuftsin conjugate, Dau-Aoa-T5(4-dec), had a similarly high internalization as the Dau-SynB3-conjugates. This salient uptake of Dau-Aoa-T5(4-dec) is reflected in its high cytostatic activity on U87 cells. We also studied the uptake of the smallest, Dau-containing metabolites produced during lysosomal degradation to get a hint about their membrane crossing ability that can be significant in their transport across intracellular membranes (e.g., membranes of lysosomes and cell nuclei). Dau-Aoa-Gly-OH showed the highest internalization rate among these metabolites. This finding is in correlation with its superior cytostatic activity after 3 h in U87 cells among the Dau-metabolites. The uptake of Dau-Aoa-Thr-OH was the lowest among the metabolites; this explains why it showed no cytotoxic activity in U87 cells. Probably this

metabolite cannot get sufficiently near its site of action when released from its parent conjugate (Dau-Aoa-TKPPR). Moreover, the very slow release of this metabolite from its parent conjugate observed in rat liver lysosomal homogenate could also be in correlation with the low antitumor efficacy of Dau-Aoa-TKPPR.

Statistical analysis (Kruskal−Wallis test with multiple comparisons) shows that both the fluorescence intensity profile and percentage of Dau+ cells of Dau-treated cells are significantly different from the profiles of the following conjugates: Dau-Aoa-T5, Dau-Aoa-GFLG-T5, Dau-Aoa-TKPPG-OT10, Dau-Aoa-TKPPR, and Dau-Aoa-Arg-OH (for details, see Table S4).

We also compared the cellular uptake of Dau-Aoa-SynB3, Dau-Aoa-TKPPR, and their tandem conjugate Dau-Aoa-SynB3-TKPPR on the MDA-MB 435Br brain metastasis cell line (Figure 7 and Figure S22). These cells internalize the SynB3-

Figure 7. Comparison of the cellular uptake of Dau-peptide conjugates at 25 μM on MDA-MB 435Br cells using flow cytometry (3 h incubation time). (A) The ratio of living, fluorescence positive cells, (B) mean intracellular fluorescence intensity of living, fluorescence positive cells, and (C) quantified value of the uptake rate (UC$_{50}$) of the conjugates. Experiments were carried out in duplicates; error bars represent standard deviation.

conjugate and the tandem conjugate to a similar extent. The cellular uptake of the tuftsin conjugate Dau-Aoa-TKPPR is very low (for statistical analysis, see Table S5).

Selected Dau-conjugates were studied in HUVECs that can be used for modeling tumor related vascular endothelial cells. As can be seen in Figure S23, Dau could enter these cells similarly as in the case of U87 cells with a very high uptake rate. Dau-SynB3 conjugates and tandem conjugates showed a superior uptake rate among the conjugates, and interestingly, the internalization rate of the tandem conjugate Dau-Aoa-SynB3-TKPPR was higher than the rate of the Dau-Aoa-SynB3 conjugate (for statistical analysis, see Table S6).

Intracellular Localization of Peptides and Conjugates. Besides the quantitative analysis of the cellular uptake by flow cytometry, the localization of peptides and conjugates was also studied in U87 cells by confocal laser scanning microscopy (CLSM). Different laser intensities were used in the case of compounds with low or high internalization to improve visualization and optimize the image quality; therefore, the CLSM observations cannot be considered as quantitative

analysis but provide qualitative information about subcellular localization. Nuclear staining with Hoechst 33342 and lysosome staining with LysoTracker Deep Red (or LysoTracker Red DND-99) was performed in order to get insight into a possible colocalization with nuclei and lysosomes. All of the experiments were carried out with 30 and 90 min of incubation time, and no significant differences were observed between the different treatment periods. Here, only representative images after a 30 min treatment time are shown; images obtained after 90 min incubation time can be found in the Supporting Information (Figures S24−S26).

First, to rule out fixation artifacts in the cellular distribution of CPPs,[90] we compared confocal images of live (unfixed, Figure S24) and fixed cells treated with Cf-peptides (Figure 8). After 30 min of incubation with Cf-peptides at 25 μM concentration, the U87 cells were directly visualized by CLSM, or the cells were fixed prior to visualization. We did not observe fixation artifacts; distribution of the peptides showed mostly identical patterns in both cases. Cf-SynB3 was located in the cytosol, in the nucleus, and in small, cytosolic compartments (vesicles that could be endosomes). A low lysosomal localization was also detected. This suggests that the uptake of this CPP is complex; not only does direct cell penetration play a role but also vesicular transport can occur.[21] In the case of Cf-TKPPR, the peptide showed predominant colocalization with lysosomes and no localization in the nucleus. This indicates that this tuftsin derivative mainly internalizes through a form of endocytosis, as expected. The Cf-SynB3-TKPPR tandem peptide could be detected both in the nucleus and in lysosomes; however, it could also be observed in the cytosol and in the proximity of the cell membrane. Presumably, Cf-SynB3-TKPPR follows the internalization mechanisms of both its CPP part and its tuftsin part, and the endolysosomal pathway is more pronounced than in the case of Cf-SynB3.

Modification of peptides with fluorophores could differently influence the biological properties of the peptides such as uptake and intracellular distribution.[89,91,92] Hence, Dau can be considered as a fluorophore; therefore, we also investigated the intracellular distribution of Dau-conjugates comparing them with the corresponding Cf-peptides and Dau itself. U87 cells were treated with Dau and Dau-conjugates at 25 μM for 30 min and the cells were fixed prior to visualization (Figure 9). As expected, Dau was mainly localized in the nucleus. In the case of the Dau-Aoa-SynB3 conjugate, the Dau signal was mainly in the nucleus and vesicular localization could also be observed; there was no significant lysosomal localization. The Dau signal was mainly in the lysosomes in the case of Dau-Aoa-TKPPR. In the case of the tandem conjugate Dau-Aoa-SynB3-TKPPR, the Dau signal was in the nucleus and in lysosomes. These results showed that the localization patterns of corresponding Cf-peptides and Dau-conjugates are mostly identical. We can conclude that the compounds that contain the SynB3 motif can enter the cell nucleus, proving that the conjugated Dau can reach its site of action; however, conjugation with the peptides decreased the nuclear localization of Dau, and this could explain the reduction of the cytotoxic activity of the conjugates. The main difference between the Cf- and Dau-peptides was that the fluorescence signal in nuclei was more prevalent in the case of Dau-Aoa-SynB3 and Dau-Aoa-SynB3-TKPPR than in the case of the corresponding Cf-peptides (namely, Cf-SynB3 and Cf-SynB3-TKPPR). This phenomenon can be explained by the fact that Dau tends to accumulate in cell nuclei; therefore, these Dau-conjugates or their Dau-containing metabolites can enter cell
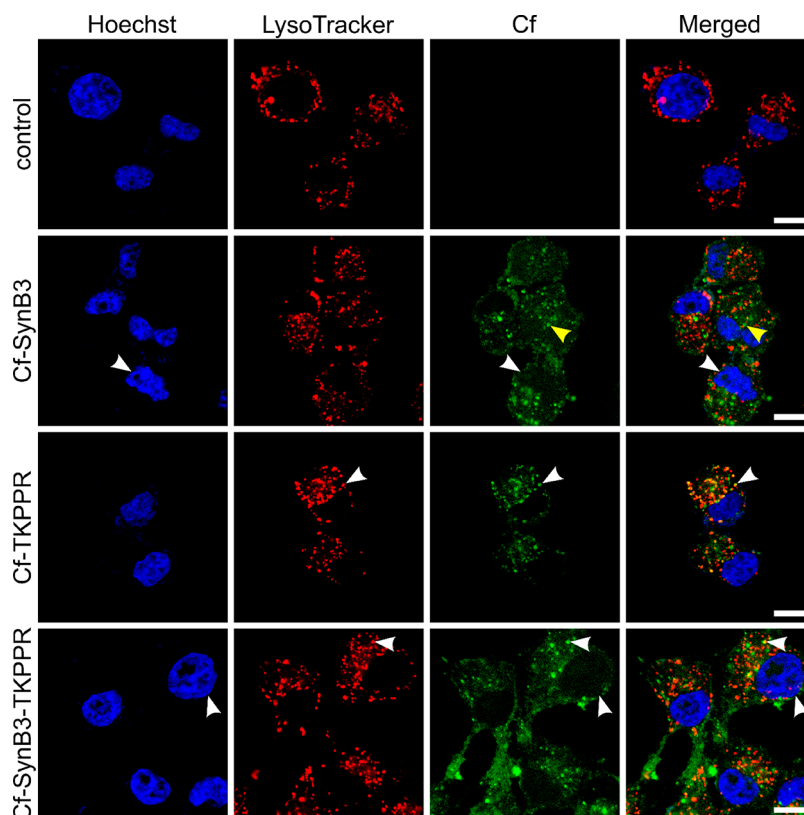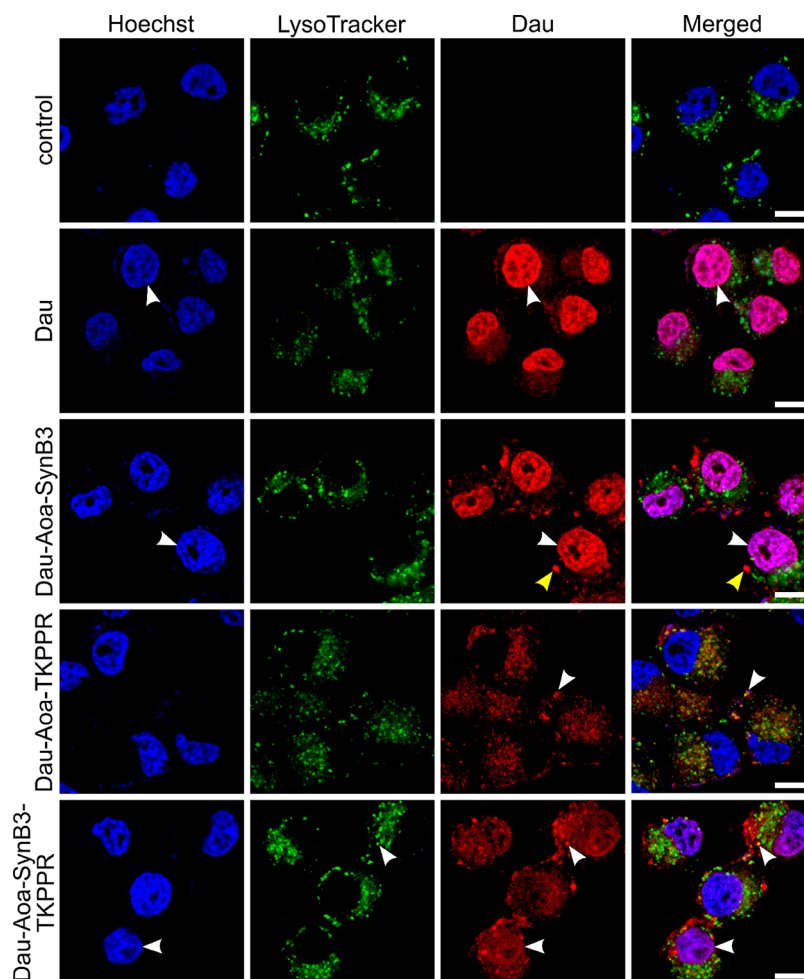
Figure 8. Localization of Cf-peptides in U87 cells (fixed) by confocal microscopy. Cells were incubated with Cf-labeled peptides (green, 25 μM, 30 min), lysosomes were stained with LysoTracker Deep Red (red), and nuclei were stained with Hoechst 33342 (blue). White arrows indicate examples of nuclear or lysosomal colocalization; yellow arrows indicate vesicular localization. The scale bar represents 10 μm.

nuclei and it is preferable, since Dau is a DNA-damage-inducing agent. Taken together with the rapid production of Dau-containing lysosomal metabolites (Dau-Aoa-Arg-OH) from these conjugates, presumably these observations contribute to their high cytostatic activity. In the case of Dau-Aoa-TKPPR, no significant accumulation of the Dau signal in the cell nucleus was observed, neither after a longer, 90 min treatment (Figure S26). After the treatment, the Dau-Aoa-TKPPR conjugate was still located in the lysosomes. The lysosomal degradation of this conjugate was slower, and it required more time to release the smallest Dau-containing metabolite. This and the finding of its low uptake rate could also be the reason for the high IC$_{50}$ value of this conjugate.

Penetration Ability of the Conjugates on Lipid Monolayer and Transwell Co-Culture with Noncontact HUVEC-U87 Monolayers as *ex Vivo* and *in Vitro* BBB Model. The monomolecular lipid membrane model was used to characterize the interactions between the lipid monolayers and the selected Dau-conjugates (Dau-Aoa-TKPPR, Dau-Aoa-SynB3, and Dau-Aoa-SynB3-TKPPR). The membrane affinity was investigated by using the Langmuir technique employing brain extract polar lipid (BEPL) in chloroform to form a monomolecular lipid layer to mimic the BBB lipid composition (Figure 10A). Despite that DPPC and DOPC monolayers are widely used as a simplified model of the mammalian cell membrane, the BEPL mixture was applied in the present membrane affinity measurements as an *ex vivo* model. This can be considered as a more realistic model to mimic the composition of central nervous system barriers and neuronal membranes.[93,94]

The change of surface pressure ($\Delta\Pi$) detected after 30 min of interaction is plotted for the Dau-conjugates (Figure 10B). All of the conjugates showed a certain membrane affinity presented by the significant increase of the surface pressure of the lipid monolayer following the appearance of the Dau-conjugate in the subphase. The degree of penetration was quite low for Dau-Aoa-TKPPR while notably higher for conjugates containing the SynB3 sequence. Although all of the three conjugates were highly polar (see calculated LogP (Figure S5) and net charges (Table S1)), the main difference which apparently influences the interaction with the BEPL layer is their charge character. The number of cationic amino acids in the conjugates is 2, 5, and 7 for Dau-Aoa-TKPPR, Dau-Aoa-SynB3, and Dau-Aoa-SynB3-TKPPR, respectively. That order corresponds to the increased interaction with the negatively charged lipid layer resulting in enhanced membrane affinity. The highest degree of penetration was observed for Dau-Aoa-SynB3-TKPPR due to its strong electrostatic attraction with charged membrane components. The membrane affinity was investigated with lipid layers compressed to 25 and also for 30 mN/m. As is expected, the degree of penetration was usually higher into a less compressed (25 mN/m) lipid layer and somewhat smaller due to steric reasons applying a more compressed layer (30 mN/m). A reverse relation was observed in our case for two conjugates, which might support the importance of electrostatic interaction. In the case of more compressed film, the charge density was also increased facilitating the electrostatic attraction of Dau-conjugates. The higher membrane affinity of the SynB3-containing Dau-conjugates observed in lipid monolayer experiments is in harmony with their conformational change in membrane mimetic solvent (i.e., increased α-helix content)

Figure 9. Localization of Dau and Dau-conjugates in U87 cells (fixed) by confocal microscopy. Cells were incubated with Dau or Dau-conjugates (red, 25 μM, 30 min), lysosomes were stained with LysoTracker Deep Red (green), and nuclei were stained with Hoechst 33342 (blue). White arrowheads indicate examples of nuclear or lysosomal colocalization; yellow arrowheads indicate vesicular localization. The scale bar represents 10 μm.

determined by CD measurements (Table 1). A similar correlation was found to be valid previously for structural and membrane interaction features of cationic CPPs.[95]
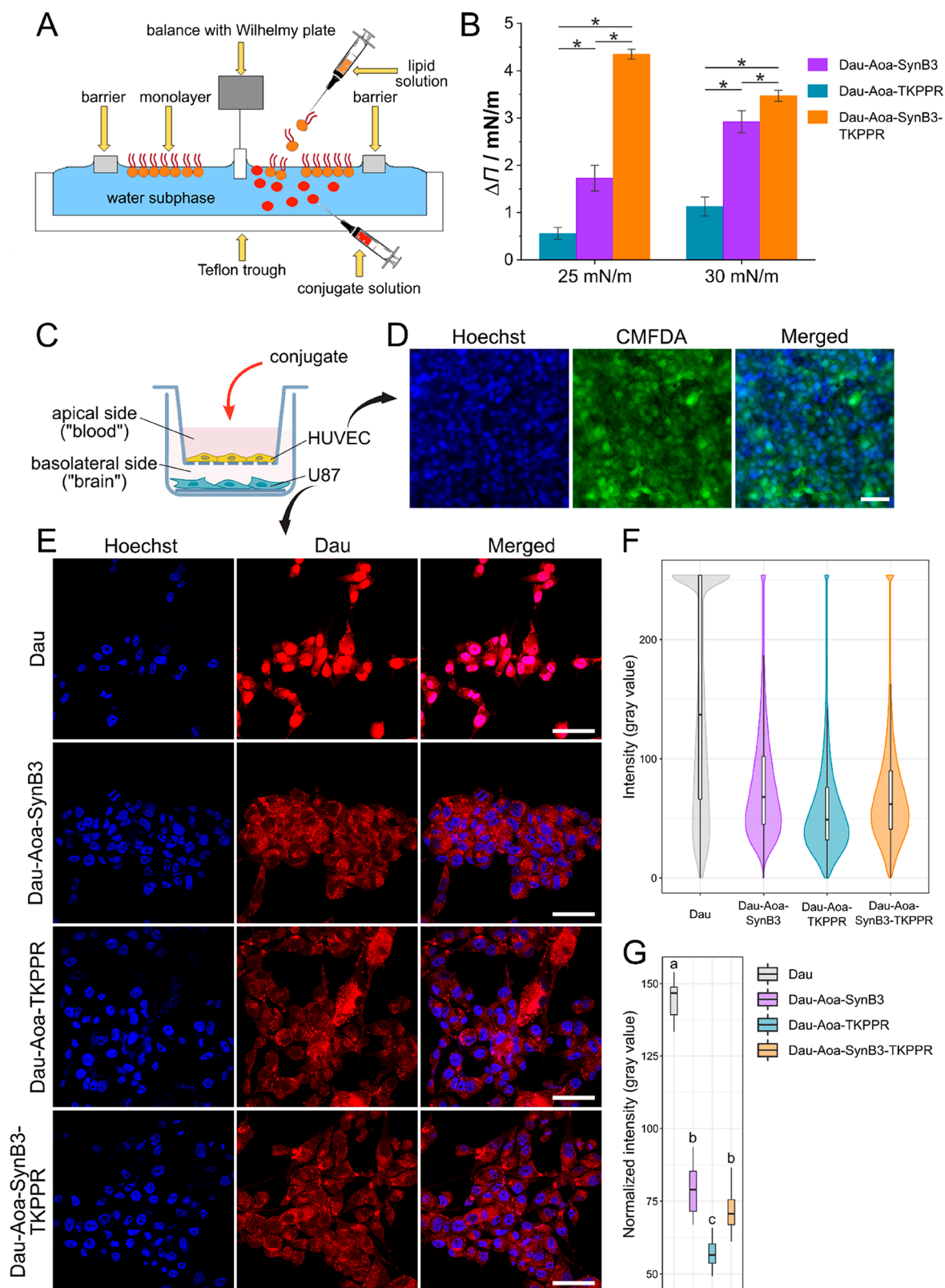
We studied the penetration ability of the conjugates on Transwell (TW) using co-cultured noncontact monolayers of HUVEC and U87 cells as a simple *in vitro* BBB model (Figure 10C,D based on ref 96). Compounds (Dau and conjugates Dau-Aoa-SynB3, Dau-Aoa-TKPPR, and Dau-Aoa-SynB3-TKPPR) were added to the HUVEC-containing apical chamber at 50 μM concentration, and after 45 min or 3 h of incubation, U87 cells from the basolateral chamber were stained and fixed prior to CLSM analysis. As control experiments, treatments without the TW were also carried out (Figure S27A,B). The same laser intensities were used in all cases, and the Dau signal in U87 cells was compared based on ImageJ analysis (Figure S27C). Dau and all three conjugates were able to cross the HUVEC monolayer, and they were internalized into U87 cells. According to the Dau signal intensity, the internalization rates followed the same pattern as obtained in the cellular uptake studies (Figure 10E−G); namely, Dau, Dau-Aoa-SynB3 and the tandem conjugate have a higher internalization rate (after crossing the membrane and HUVEC barrier) than the tuftsin conjugate. Similar tendencies were observed after 3 h of incubation (data not shown).

3D Tumor Spheroids as Platforms to Study the Penetration Profile of Peptide Carriers. Two-dimensional (2D) monolayer cultures are leading, well-established and reproducible models to assay on *in vitro* functional responses, structure−activity relations. However, cells grown in 2D form lack cell−cell and cell−extracellular matrix interactions. In comparison with monolayers, three-dimensional (3D) cultures are more analogous to *in vivo* environments. The 3D platforms can eliminate the species differences in contrast with animal models. Other differences manifest in cell morphology, cell−cell and cell−matrix interactions, gene expression, and differentiation.[97] *In vitro* 3D cell cultures offer more accurate models to mimic multicellular complexity, transport processes, and biochemical factor gradients of solid tumors *in vivo* than cells in 2D monolayers.[4,5]

The poor penetration of drugs into tumor tissues could be associated with low therapeutic efficacy and recurrence of tumors. In our approach, we used a simple, anchorage-independent 3D culture form,[98] a spheroid model for assaying the drug-conjugates. The workflow of the preparation, treatment, imaging, and analysis of 3D tumor spheroids can be seen in Figure 11.

Penetration Profile of Drug Conjugates in 3D Tumor Spheroids. We compared the penetration ability of Dau and three Dau-peptide conjugates, namely, Dau-Aoa-SynB3, Dau-

Figure 10. The penetration ability of conjugates was assessed tensiometrically employing a Langmuir balance. (A) Schematic representation of the drug penetration studies using a Langmuir monolayer. (B) The degree of penetration ($\Delta\Pi$) of the selected Dau-conjugates into the BEPL monolayer after 30 min of interaction. Error bars represent the confidence intervals (95%) of the determined mean values calculated using Student's t test from three parallel measurements ($p < 0.05$). (C) Schematic representation of the Transwell co-culture arrangement with noncontact monolayers as the BBB model containing HUVEC and U87 cells. HUVECs were seeded on the apical side of the TW insert, and U87 cells were seeded on the basolateral chamber employing coverslips. (D) Microscopic images of the HUVEC monolayer on the TW membrane; nuclei were stained with Hoechst 33342 (blue), the cytoplasm of the cells was stained with CMFDA (green), and the scale bar represents 50 μm. (E) CLSM images of U87 cells from the *in vitro* TW model, where Dau and Dau-conjugates (red, 50 μM, 45 min incubation) were added to the apical chamber. Nuclei of U87 cells from the

Figure 10. continued

basolateral chamber on coverslips were stained with Hoechst 33342 (blue); cells were fixed and analyzed by CLSM. The scale bar represents 50 μm. (F) Violin plots of intensity values derived from CLSM images of U87 cells from the *in vitro* Transwell model, where Dau or Dau-conjugates were added to the apical chamber. The overlaid box-and-whisker plots show the median (horizontal line), the interquartile range (box), and minimum and maximum values (whiskers) of intensity according to the field of view (every inner pixel). (G) The results of the statistical analysis of the mean normalized intensity values of cell clusters treated with Dau or Dau-conjugates. Box-and-whisker plots show the median (horizontal line), the interquartile range (box), and minimum and maximum values (whiskers) of intensity values. Letters demonstrate the results of Tukey's procedure for all-pairwise comparisons based on the one-way ANOVA ($F(3,33) = 134.6$; $p < 0.001$); different letters mean significant differences at $p < 0.05$.
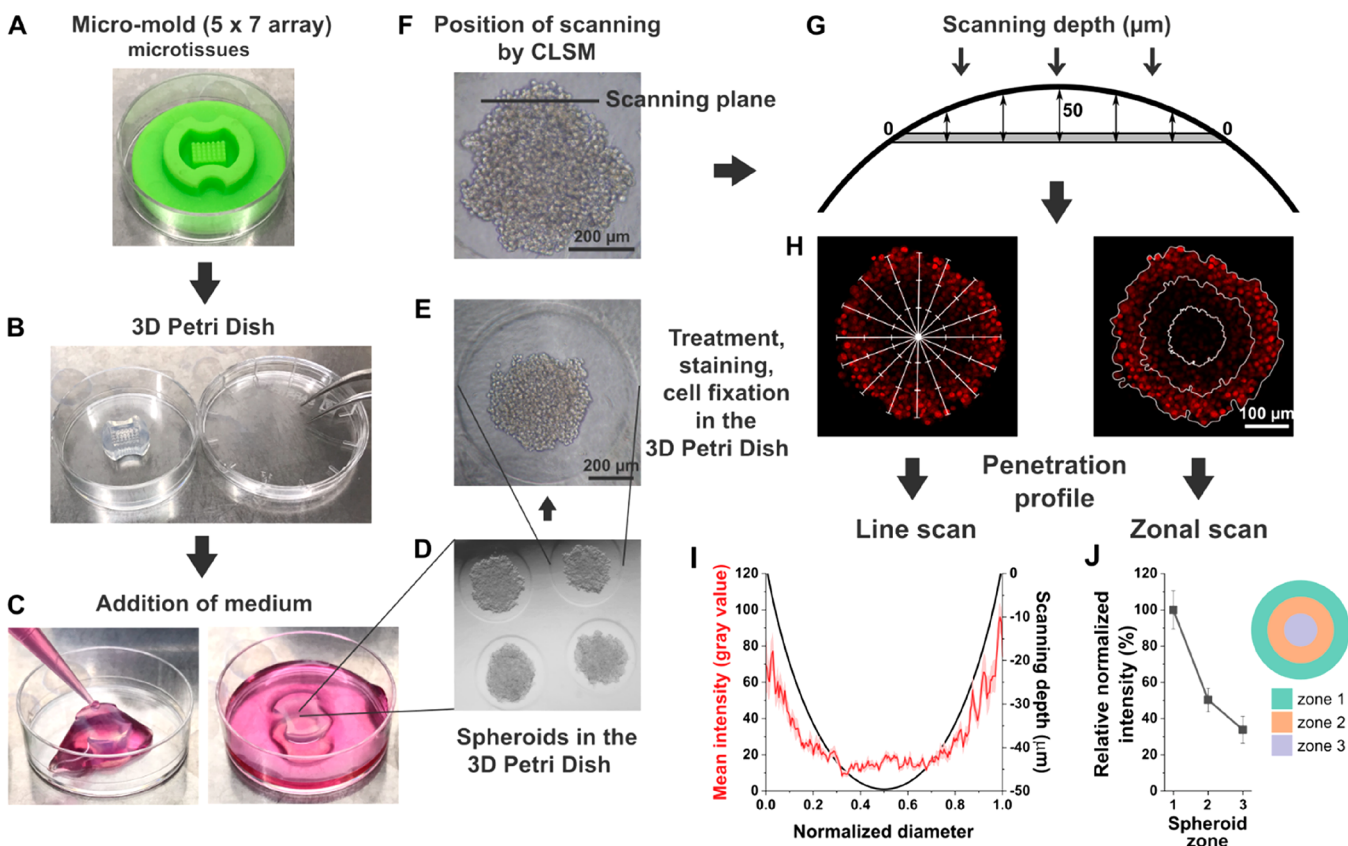
Figure 11. Workflow of preparation, treatment, imaging, and analysis of 3D tumor spheroids. (A) Micromold used for casting of a 3D Petri dish (microtissues), (B) 3D Petri dish in a 35 mm Petri dish, (C) addition of complete cell medium, (D) view of tumor spheroids in a 3D Petri dish, (E) treatment, nucleus staining, and cell fixation performed inside the 3D Petri dish, (F, G) side-view of a tumor spheroid with the position of the scanning plane during CLSM imaging (section z5, corresponding to the z-section captured 50 μm from the surface), (H) position of lines during line scan and position of zones for zonal scan of section z5 of spheroids (two parallel spheroids, 8 lines and 3 zones each), (I) penetration profile by line scan, mean intensity (red line), and SEM (light-red error stripe) averaged from gray values (0−255) of 16 parallel line scans and depth of scanning (black line) along the normalized spheroid diameter, (J) penetration profile by zonal scan; spheroids were separated into a peripheral (zone 1), intermediate (zone 2), and core zone (zone 3), and the relative normalized intensity was determined.

Aoa-TKPPR, and Dau-Aoa-SynB3-TKPPR. Spheroids formed from U87 glioma cells or MDA-MB 435Br were treated with the compounds for 3 h at 25 μM concentration. Nuclear staining with Hoechst 33342 was also applied. Fixed spheroids were visualized by CLSM. A lower laser intensity was used in the case of Dau and higher but the same intensity in the case of the three Dau-conjugates to improve visualization and to optimize the image quality; therefore, the CLSM observations cannot be considered as quantitative analysis but provide qualitative information about the penetration ability. The U87 and MDA-MB 435Br spheroids had an average diameter of 500 and 400 nm, respectively (Figure S28). To compare the penetration profile of the compounds, we have preformed line scan analysis and zonal scan analysis of the spheroids. Spheroids were scanned in the z-direction with a step size of 10 μm (z1−z7). The deepest
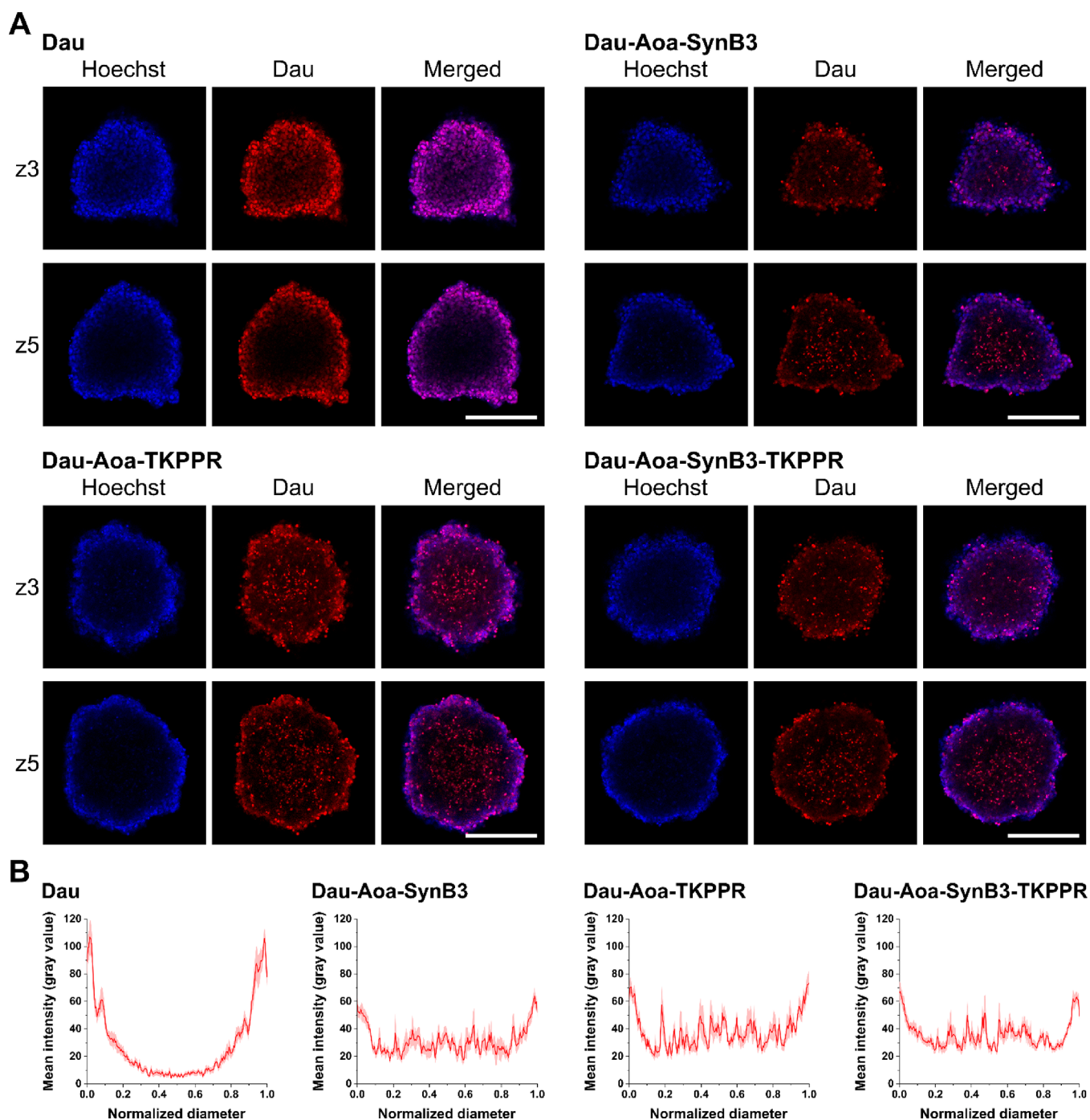
z-section from the surface of a spheroid presented here is 50 μm (z5). Deeper sections were also recorded; however, a z5 section was chosen as a z-section where the conjugates are securely visible by the objective used during microscopic imaging. For the comparison of sections z1−z7 with line scan analysis, see Figure S29. However, at this depth (between 10 μm (z1) and 50 μm (z5)), we managed to observe the differences between the penetration ability of Dau and its conjugates. Two z-sections (z3 with depth of 30 μm and z5 with depth of 50 μm) of U87 and MDA-MB 435Br spheroids are shown in Figure 12A and Figure 13A, respectively. The first five z-sections can be seen in Figure S30 for U87 spheroids and in Figure S31 for MDA-MB 435Br spheroids. In both cases, we observed that the Dau and even the Hoechst 33342 nuclear stain could not successfully penetrate into deeper layers; they were mostly localized at the spheroid
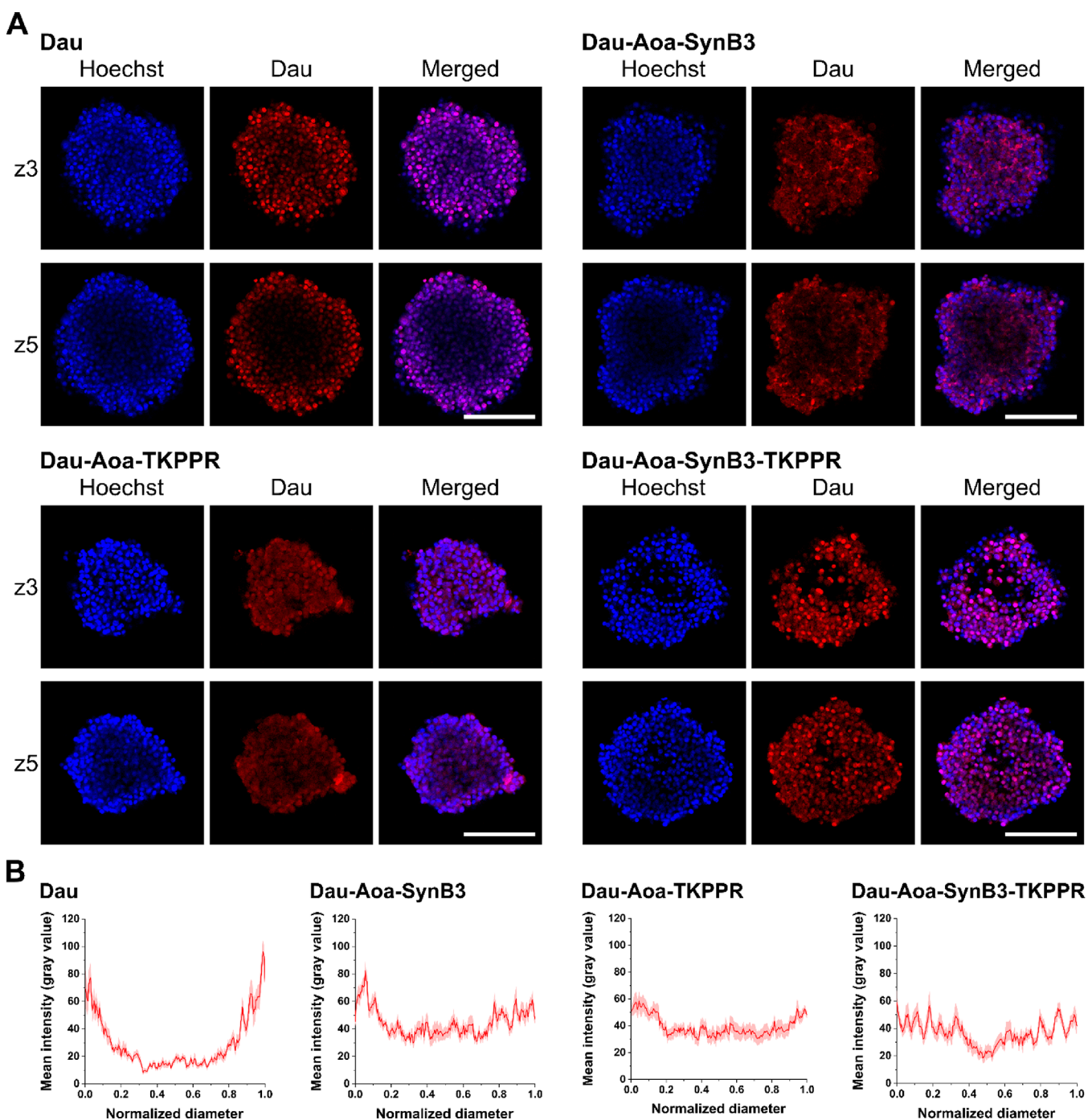
Figure 12. (A) Representative confocal images of U87 spheroids after 3 h treatment with 25 μM Dau or Dau-peptide conjugates (red). Nuclei were stained with Hoechst 33342 (blue). Z-stack images were obtained starting at the surface of the spheroid with 10 μm intervals for a total of 50 μm into the spheroid; the presented images are from the 30 μm (z3) and 50 μm (z5) depths. The scale bar represents 200 μm. (B) Line scans of spheroids at 50 μm (z5) depth; mean intensities are gray values (0−255) averaged from two parallel spheroids (n = 16 line scans), and error stripes correspond to SEM.

surface. Toward the center of the spheroids, the Dau and Hoechst 33342 signal was gradually decreasing. On the contrary, in the case of the Dau-conjugates, the Dau signal could be observed closer to the center. Line scans of z5-section images (Figure 12B and Figure 13B) also confirm these observations, as we can see the differences between the steepness of the mean gray value lines. The mean gray value of the conjugates only slightly decreased toward the middle of the spheroids, while free Dau started with a high mean gray value at the spheroid surface,

and this value showed a steeper decrease toward the spheroid center. In the case of zonal scan analysis, the spheroids were divided into different zones (periphery (zone 1), intermediate (zone 2), core (zone 3)) using equal steps from the surface of the spheroids. To have comparable fluorescent intensity values among the treatments and zones, normalized gray value data were standardized as the proportion of the mean normalized intensity in the peripheries (0−100%). The zonal penetration profile comparing the relative normalized intensities also

A

Dau

Hoechst	Dau	Merged

Dau-Aoa-SynB3

Hoechst	Dau	Merged

Dau-Aoa-TKPPR

Hoechst	Dau	Merged

Dau-Aoa-SynB3-TKPPR

Hoechst	Dau	Merged

B

Figure 13. (A) Representative confocal images of MDA-MB 435Br spheroids after 3 h treatment with 25 μM Dau or Dau-peptide conjugates (red). Nuclei were stained with Hoechst 33342 (blue). Z-stack images were obtained starting at the surface of the spheroid with 10 μm intervals for a total of 50 μm into the spheroid; the presented images are from the 30 μm (z3) and 50 μm (z5) depths. The scale bar represents 200 μm. (B) Line scans of spheroids at 50 μm (z5) depth; mean intensities are gray values (0−255) averaged from two parallel spheroids ($n = 16$ line scans), and error stripes correspond to SEM.

supports the difference between Dau and the Dau-conjugates (Figure 14; for the statistical analysis combining the line and zonal scan data sets, see Figure S32 and Table S7). Based on these results, we can conclude that all three conjugates have an improved penetration ability compared to the free Dau on both types of spheroids. Conjugation of Dau to peptide carriers significantly enhanced the *in vitro* penetration ability on the spheroid model.

■ CONCLUSIONS

Current chemotherapeutics can be very effective on glioma cell growth inhibition, but unfortunately, their cellular internalization rate and BBB penetration ability are limited. Finding new delivery vehicles and strategies to increase drug internalization in the glioma tissue is an urgent need. In this study, we focused on establishing delivery peptides. Therefore, we designed and prepared new peptide conjugates employing different antiglioma agents such as salicylanilides, Dau, and TMZ. As carrier
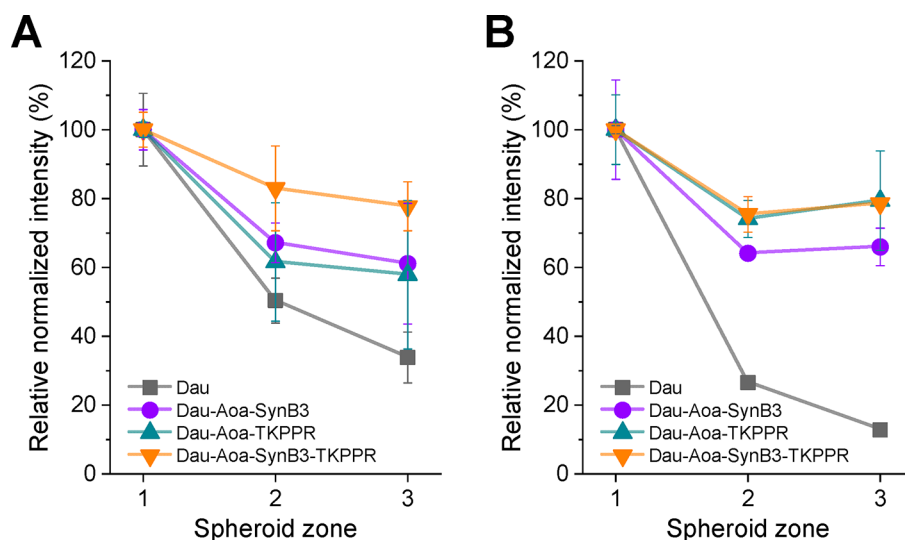
Figure 14. Relative normalized intensity of spheroid zone 1, zone 2, and zone 3 displaying the penetration ability of the Dau and Dau-conjugates in (A) U87 spheroids and in (B) MDA-MB 435Br spheroids. Relative normalized intensities of spheroids were extracted at 50 μm (z5) depth, averaged from two parallel spheroids (n = 2); error stripes correspond to SEM.

peptides, derivatives of SynB3 cell-penetrating peptide with the ability to cross the BBB were employed. Tuftsin derivatives were also used as carriers with the aim of targeting the NRP-1 transport system to achieve selectivity and better tumor penetration. Moreover, we combined the two types of carriers to create SynB3-tuftsin tandem peptides to exploit their advantageous properties.

As our study demonstrated, the salicylanilide derivatives have good cytostatic activity against U87 cells and the salicylanilide-SynB3 conjugates are also active against this cell culture. Dau-conjugates have superior antitumor activity to Sal3-conjugates. Interestingly, the CendR-motif-containing Dau-Aoa-TKPPR is the least effective among Dau-conjugates with moderate cytostatic activity. The activity of the tandem Dau-conjugates is good; it is between the activity of Dau-Aoa-SynB3 and the corresponding tuftsin conjugates. Importantly, in contrast with the free drugs, the Sal3- and Dau-conjugates proved to be selective for tumor cells, as they show no cytotoxic effect on HUVECs.

We revealed further aspects regarding the structure−activity relationship of the conjugates. The secondary structure, cellular uptake, intracellular localization, and release of the smallest, drug-containing metabolite also play an important role in their activity. Specifically, the internalization rate on 2D cell cultures of SynB3 and tandem derivatives is outstanding and significantly higher than the internalization rate of most tuftsin derivatives that is in line with their ability of forming helices upon contact with lipid membranes. The release of the smallest Dau-metabolite from Dau-SynB3 conjugates or Dau-tandem conjugate is fast; moreover, the conjugates or Dau-containing metabolites can be found in the nuclei, at the site of their action. On the other hand, Dau-Aoa-TKPPR shows a low and slow uptake rate, nuclear localization is not observed, and the release of the Dau-metabolite is very slow which contributes to its lower cytostatic activity. This conjugate shows lysosomal localization as a result of endocytosis. The Dau-Aoa-SynB3-TKPPR tandem conjugate follows the internalization mechanisms of both its CPP part and its tuftsin part, since it can be observed in cell nuclei as well as in lysosomes.

To elucidate the penetration ability of the conjugates, *ex vivo* monolayer using Langmuir balance and *in vitro* Transwell measurements using co-cultured noncontact monolayers of HUVEC and U87 cells as a simple BBB model were performed. All of the Dau-conjugates show membrane affinity on the BEPL mixture, and they are able to cross the HUVEC monolayer and enter U87 cells. Furthermore, using 3D spheroid cultures for modeling solid tumors *in vitro*, we have demonstrated that Dau-conjugates have better *in vitro* tumor penetration ability than the free Dau itself. These experimental setups provided a remarkable difference of the internalization pattern between free Dau and Dau-conjugates on cell monolayers and the spheroid model. To compare the penetration and internalization capacity of the conjugates, we have employed CLSM line and zonal scans as enumeration for differences, but we need to emphasize that these observations can be considered as qualitative information. Taken together, using these peptides as carriers, significantly improved penetration ability can be obtained. The applied cell monolayers, co-culture system, and tumor spheroids were suitable *in vitro* models in order to find the most promising constructs for *in vivo* studies. In conclusion, drug-peptide conjugates presented here, in particular Dau-Aoa-SynB3-TKPPR, are promising constructs toward the rational design of glioma targeting using tandem peptide based delivery vehicles to achieve better antitumor efficiency, cellular uptake, and, most importantly, a superior tumor penetration ability.

■ EXPERIMENTAL SECTION

Materials. Amino acid derivatives and resins were purchased from Iris Biotech GmBH (Marktredwitz, Germany). Boc-aminooxyacetic acid (Boc-Aoa-OH), 1-hydroxybenzotriazole hydrate (HOBt), N,N'-diisopropylcarbodiimide (DIC), triisopropylsilane (TIS), phenol, thioanisole, 1,2-ethanedithiol (EDT), piperidine, 1,8-diazabicyclo[5.4.0]undec-7-ene (DBU), N,N-diisopropyl-N-ethyl-amine (DIEA), benzotriazole-1-yl-oxy-tris-pyrrolidino-phosphonium hexafluorophosphate (PyBOP), acetic anhydride (Ac$_2$O), acetic acid (AcOH), 5(6)-carboxyfluorescein (Cf), temozolomide (TMZ), trifluoroethanol (TFE), and acetonitrile were purchased from Sigma-Aldrich (Budapest, Hungary). Trifluoroacetic acid (TFA), N,N-dimethylformamide (DMF), dichloromethane (DCM), methanol, chloroform, and diethyl ether were purchased from VWR (Budapest,

Hungary). Daunomycin hydrochloride was a gift from IVAX (Budapest, Hungary). All reagents and solvents were of analytical grade or highest available purity and were used without further purification. Dulbecco's Modified Eagle Medium (DMEM) was from Lonza (Basel, Switzerland), and RPMI-1640 medium, fetal bovine serum (FBS), Mowiol 4-88, trypan blue, and trypsin were obtained from Sigma-Aldrich. HPMI buffer (9 mM glucose, 10 mM $NaHCO_3$, 119 mM NaCl, 9 mM HEPES, 5 mM KCl, 0.85 mM $MgCl_2$, 0.053 mM $CaCl_2$, 5 mM $Na_2HPO_4 \cdot 2H_2O$, pH 7.4) was prepared in-house using components obtained from Sigma-Aldrich.

Synthetic Procedure. Synthesis and characterization of salicylanilides (Sal1, Sal2, Sal3) is presented in refs [50] and [63]. Temozolomide-carboxylic acid was prepared following a previously described procedure.[70,71]

Peptides were synthesized manually on the solid phase (Fmoc-Rink Amide MBHA resin for peptides with C-terminal in amide form and Wang resin for peptides with C-terminal in carboxyl form) using the Fmoc/*t*Bu strategy with DIC/HOBt coupling reagents, as described previously.[50] Acetylated derivatives were produced by acetylation of the N-terminal using acetic anhydride/DIEA/DMF (1:1:2 v/v, 60 min). Fluorescently labeled derivatives were prepared with the use of 5(6)-carboxyfluorescein (Cf) with the DIC/HOBt coupling method. In the case of decanoyl-containing peptides, in the required position, lysine was built in as an Fmoc-Lys(Dde)-OH protected form. After the final Fmoc-deprotection, Boc-Aoa-OH or Cf was coupled to the N-terminal of the peptides (DIC/HOBt coupling method) or the N-terminal was acetylated. After the derivatization of the N-terminal, the Dde protecting group was selectively removed with 2% hydrazine hydrate in DMF (v/v) (6 × 2 min); then, decanoic acid was reacted with the free ε-amino group of the Lys residue in the presence of DIC/HOBt coupling reagents. In the case of the decanoyl-containing peptide that has free amino group at the N-terminal (H-SynB3K(dec)), the Dde protecting group was removed and decanoic acid was coupled before the removal of the final N-terminal Fmoc-protecting group. Peptides without Arg were cleaved from the resin with TFA/H_2O/TIS (95:2.5:2.5 v/v) mixture (2.5 h, RT). After filtration, compounds were precipitated in cold diethyl ether, centrifuged (4000 rpm, 5 min), and freeze-dried from water. Arg-containing peptides were cleaved from the resin with TFA/thioanisole/H_2O/EDT/phenol (82.5:5:5:2.5:5 v/v/v/v/w) mixture (2.5 h, RT). In the case of SynB3 derivatives (five or six Arg in the sequence) during cleavage, the cleavage product of the Arg side chain protecting group (Pbf) was precipitated. Therefore, diethyl ether was added to the reaction mixture to dissolve the precipitated side chain cleavage product and to precipitate the peptide. This mixture was centrifuged (4000 rpm, 5 min), and the peptide was dissolved in 10% AcOH in water (v/v), filtered off from the resin, and freeze-dried from 10% AcOH in water (v/v). The (aminooxy)acetyl-amino acid derivatives (Aoa-Arg-OH, Aoa-Gly-OH, Aoa-Thr-OH) were synthesized by solid-phase peptide synthesis on Wang resin manually using the Fmoc/*t*Bu strategy as described previously.[50]

Sal3 and Dau were conjugated to the (aminooxy)acetylated peptides or amino acids through an oxime bond.[50] Crude Aoa-peptides and Aoa-amino acid derivatives were used for conjugation without purification. The oxime bond formation was carried out under acidic conditions (pH 4.5) in a mixture of 0.2 M sodium acetate buffer and 2-methoxyethanol for Sal3 conjugation, at a peptide concentration of 5−10 mg/mL. Sal3 was used in 10% molar excess as compared to the Aoa-peptides. In the case of Dau-conjugates, oxime bond formation was carried out in 0.2 M ammonium acetate buffer (pH 5.0) with a 10% molar excess of Dau. The reaction mixtures were stirred for 3−72 h at room temperature and monitored by analytical RP-HPLC.

TMZ conjugates were synthesized on the solid phase. Temozolomide-carboxylic acid (TMZA) was coupled to the free N-terminal of the peptides (SynB3 and GFLG-SynB3) on the resin forming amide bond. Four equivalents (calculated to the resin capacity) of TMZA, PyBOP, and DIEA dissolved in DMF was used for coupling for 4 h at RT. The coupling reaction was verified by ninhydrin test, and the conjugates were cleaved from the resin as described above.

Reverse-Phase High-Performance Liquid Chromatography (RP-HPLC). The crude peptides and conjugates were purified on a

KNAUER 2501 HPLC system (H. Knauer, Bad Homburg, Germany) using a semipreparative Phenomenex Jupiter Proteo C12 column (10 mm, 90 Å, 10 × 250 mm) (Torrance, CA, USA). The applied flow rate was 4 mL/min at ambient temperature, and the peaks were detected at 220 nm. Gradient elution was used with the following eluents: 0.1% TFA/water v/v (eluent A), 0.1% TFA/acetonitrile−water 80:20 v/v (eluent B). Analytical RP-HPLC was performed on an Exformma HPLC system (EX1600 Wufeng Scientific Instruments, Sanghai, China) using a Waters Symmetry C18 column (5 μm, 100 Å, 4.6 mm × 150 mm) with the following gradient: 0−5 min 0% B, 5−15 min 0−60% B, 15−25 min 60−100% B, 25−29 min 100%. The flow rate was 1 mL/min at ambient temperature, and the peaks were detected at 220 nm. All purified compounds demonstrated a single peak on analytical RP-HPLC (purity is >95%).

Electrospray Ionization Mass Spectrometry (ESI-MS). Measured monoisotopic or average molecular mass was acquired by a Bruker Esquire 3000+ electrospray ionization (ESI) ion trap mass spectrometer (Bremen, Germany) operating in continuous sample injection mode at 10 μL/min flow rate. Samples were dissolved in acetonitrile−water (50:50, v/v), containing 0.1% acetic acid. Dau-conjugate-containing samples were dissolved in 50 mM NH_4OAc buffer (pH 6.7)−acetonitrile (50:50, v/v). Mass spectra were recorded in positive ion mode in the 50−1500 *m/z* range.

Circular Dichroism (CD) Spectroscopy and Secondary Structure Analysis. Peptide samples were dissolved in deionized water and in TFE at 17−170 μM concentrations. Far-UV CD curves were taken on a JASCO J-715 spectropolarimeter at 25 ± 0.2 °C in a 0.1 cm path-length rectangular quartz cuvette (Hellma, USA). Temperature control was provided by a Peltier thermostat. The CD data were monitored in continuous scanning mode between 185 and 260 nm at a rate of 50 nm/min, with a step size of 0.1 nm, response time of 2 s, eight accumulations, and a 2 nm bandwidth. The CD curves were corrected by background contribution of the blank solvent. CD values were plotted in mean residue molar CD units ($\Delta\varepsilon$/residue) calculated by the following equation: $\Delta\varepsilon = \Theta/(32.98cl)$, where Θ is the measured ellipticity (deg) as a function of wavelength (nm), c is the mean residue molar concentration, and l is the optical path length (cm).

The contribution of the different conformational elements was estimated from the CD spectra by using the MS Excel version of the PEPFIT program developed originally by Reed and Reed.[99,100] The algorithm calculates the percentage of secondary contents (α-helix, β-sheet, disordered, and various turn types) by fitting experimental CD data to the combination of reference spectra. The best fit is defined by the R^2 value, where $R^2 = 1$ corresponds to a perfect match.

Lysosomal Digestion Profile of Conjugates in Rat Liver Lysosomal Homogenate and LC-MS Analysis. The rat liver lysosomal homogenate was prepared as described previously.[79] The degradation of the conjugates in the rat liver lysosomal homogenate was determined as follows: 90 μL of 50 μM (50 pmol/μL) conjugate solutions was prepared with 0.2 M sodium acetate buffer, pH 5.0, and the appropriate amount of lysosomal homogenate was added to them to get the conjugates:lysosomal homogenate ratio = 1:1, w/w. The reaction mixtures were incubated at 37 °C, and aliquots of 13 μL were taken after 5 min, 1 h, 2 h, 4 h, 8 h, and 24 h. The reactions were quenched by adding 2 μL of acetic acid and followed by LC-MS analysis. Control experiments were performed with solutions of conjugates in 0.2 M sodium acetate buffer, pH 5.0, with 50 μM conjugate concentration. Lysosomal homogenate control in 0.2 M sodium acetate buffer, pH 5.0, without conjugate was also prepared. Both solutions were incubated at 37 °C for 24 h and also analyzed by LC-MS. LC-MS analyses were performed on a Q Exactive Focus, high resolution and high mass accuracy, hybrid quadrupole-orbitrap mass spectrometer (Thermo Fisher Scientific, Bremen, Germany) using online UHPLC coupling. Separation was performed on a Dionex 3000 UHPLC system using a Supelco 581302-U Ascentis C18 column (2.1 mm × 150 mm, 3 μm, 100 Å). Linear gradient elution (0−2 min 2% B, 2−26 min 2−90% B, 26−27 min 90−100% B) with eluent A (0.1% HCOOH in water, v/v) and eluent B (0.1% HCOOH in acetonitrile− water, 80:20, v/v) was used at a flow rate of 0.2 mL/min at 40 °C. High resolution mass spectra were acquired in the 200−1600 *m/z* range. LC-

MS data were analyzed by Xcalibur software (Thermo Fisher Scientific) and with OriginPro 2018 (OriginLab Corporation, Northampton, MA, USA).

Cell Cultures. The following cell cultures were used for the cytostasis and cytotoxicity studies: U87 (ATCC HTB-14), MDA-MB 435Br (obtained from Janet E. Price),[80] HUVEC (isolated at the 3rd Department of Medicine Research Laboratory, Semmelweis University, Budapest, Hungary), MonoMac6 (DSMZ no.: ACC 124), and HepG2 (ATCC HB-8065). U87 and MDA-MB 435Br were maintained in DMEM medium (Lonza) supplemented with 10% FBS (Gibco, Thermo Fisher Scientific, Waltham, MA, USA) and with 2 mM L-glutamine (Lonza), 1% nonessential amino acids (Gibco), 1 mM sodium pyruvate (Sigma-Aldrich), 1% penicillin-streptomycin (from 10,000 units of penicillin and 10 mg of streptomycin/mL, Gibco). MonoMac6 and HepG2 were maintained in RPMI-1640 medium (Lonza) containing 10% FBS supplemented with 2 mM L-glutamine and 160 μg/mL gentamicin (for MonoMac6), or 1% penicillin-streptomycin (for HepG2). HUVEC was maintained in MCDB medium (90% MCDB-131 (Gibco), 5% FBS, 1% penicillin-streptomycin solution (from 10,000 units of penicillin and 10 mg of streptomycin/mL, Sigma-Aldrich), 1% Chemically Defined Lipid Concentrate from Gibco, 1% HEPES, 1% L-glutamine solution (from CTS GlutaMAX-I Supplement, Gibco), 1 ng/mL FGF-Basic (Sigma-Aldrich), 0.3% ITS (insulin-transferrin-selenium, Gibco), 2 ng/mL EGF-2 (Gibco), 7.5 U/mL heparin (Sigma-Aldrich), 5 μg/mL L-ascorbic acid (Sigma-Aldrich), 250 nM hydrocortisone). No mycoplasma contamination was detected in the cell cultures.

Determination of *in Vitro* Cytostatic and Cytotoxic Activity. U87, MDA-MB 435Br, MonoMac6, and HepG2 were plated on 96-well plates 1 day before the treatment (5000 cells/100 μL of medium/well for cytostasis and 10,000 cells/100 μL of medium/well for cytotoxicity studies). After 24 h of incubation at 37 °C, cells were treated with the compounds dissolved in serum free medium (c_{DMSO} = 1.0% v/v) at 1.3 × 10^{-3} to 100 μM concentration range and incubated for 3 or 24 h (37 °C, 5% CO$_2$). Control cells were treated with serum free medium only or with DMSO-containing serum free medium (c_{DMSO} = 1.0% v/v). After the incubation, cells were washed twice with serum free medium (centrifugation: 1000 rpm, 5 min). To determine the *in vitro* cytostatic effects, cells were cultured for a further 72 h in serum-containing medium and then the MTT assay was carried out. In the case of cytotoxicity studies, the MTT assay was performed immediately after the washing step. Cell viability was determined with (4,5-dimethylthiazol-2-yl)-2,5-diphenyltetrazolium bromide (MTT) assay. A 45 μL portion of MTT solution (2 mg/mL) was added to each well (final concentration 367 μg/mL), and during 3.5 h of incubation (37 °C, 5% CO$_2$), purple formazan crystals were formed by mitochondrial dehydrogenase enzyme present in the living cells. After incubation, cells were centrifuged for 5 min at 2000 rpm and the supernatant was removed. The obtained formazan crystals were dissolved in DMSO, and the optical density (OD) of the samples was determined at 540 and 620 nm using an ELISA Reader (Labsystems iEMS reader, Helsinki, Finland). The OD$_{620}$ values were subtracted from the OD$_{540}$ values. The percentage of cytostasis or cytotoxicity was calculated using the following equation: cytostatic or cytotoxic effect (%) = 100 × [1 − (OD$_{treated}$/OD$_{control}$)], where OD$_{treated}$ and OD$_{control}$ correspond to the optical densities of treated and control cells, respectively. In each case, two independent experiments were carried out with four parallel measurements. The 50% inhibitory concentration (IC$_{50}$) values were determined from the dose−response curves. The curves were defined using OriginPro 2018 software.

HUVEC was plated on 0.5% gelatin/PBS (v/v) pretreated 96-well plates 1 day before the experiment in MBCD medium. After 24 h of incubation at 37 °C, the confluent cells were treated with the compounds for 24 h at 3.7−100 μM concentration range. After the incubation, cells were washed with PBS to remove nonadherent cells and then fixed with ice cold methanol/acetone (1:1, v/v) for 5 min and the cell nuclei were stained with SYBR-Green I (Sigma) for 15 min followed by washing with PBS. In each case, two independent experiments were carried out with three parallel measurements. IC$_{50}$

was determined by morphological and fluorescent analysis of the cells using CellProfiler software.

Cellular Uptake Studies. Cellular uptake of fluorescent compounds was determined by flow cytometry on U87, MDA-MB 435Br, and HUVEC cell cultures. U87 and MDA-MB 435Br cells were harvested in the logarithmic phase of growth and plated on a 24-well tissue culture plate (10^5 cells/1 mL of medium/well) 24 h prior to the experiment. HUVEC was plated on 0.5% gelatin/PBS (v/v) pretreated 24-well plates 1 day before the experiment in MBCD medium to reach confluence. After 24 h of incubation at 37 °C, U87, MDA-MB 435Br, or HUVEC cells were treated with the compounds dissolved in 500 μL of serum free medium at the 0.1−50 μM concentration range and incubated for 3 h (37 °C, 5% CO$_2$). In the case of the time dependence study, U87 cells were incubated for 5 min, 15 min, 30 min, 1 h, 1.5 h, and 3 h. Control cells were treated with serum free medium only. After incubation, cells were centrifuged (1000 rpm, 5 min) and washed with serum free medium, the supernatant was removed, and 100 μL of 0.25% trypsin was added to the cells. After 3 min of incubation at 37 °C, trypsin was inactivated by 800 μL of HPMI medium containing 10% FBS, and the cells were transferred from the plate to the tubes. Cells were centrifuged (1000 rpm, 5 min), and the supernatant was removed. After this procedure, cells were resuspended in 300 μL of HPMI, and their intracellular fluorescence intensity was measured on a BD LSR II flow cytometer (BD Biosciences, San Jose, CA, USA) using a 488 nm laser (Coherent Sapphire, 22 mW) with an FITC channel for Cf-peptides (emission at 505 nm) and PE channel for Dau-conjugates (emission at 550 nm). Data were analyzed with FACSDiva 5.0 software (BD Biosciences, San Jose, CA, USA). All experiments were performed in duplicates. The 50% uptake concentration (UC$_{50}$) values were determined from the curves of the dose rate of fluorescence positive cells. The IC$_{50}$ values were determined from the curves of the dose rate of all living cells (including fluorescent positive and negative cells). The curves were defined using OriginPro 2018 software.

Confocal Microscopy Imaging. Intracellular localization was visualized by confocal microscopy. U87 cells were seeded (75,000 cells/well) in complete DMEM cell culture medium 1 day prior to treatment on cover glasses (Assistent, Karl Hecht GmbH & Co KG, Sondheim/Rhön Germany) and inserted in 24-well plates (Sarstedt, Nümbrecht, Germany). Lysosomes were stained with LysoTracker Deep Red (Invitrogen, Carlsbad, CA, USA) for 30 min (300 nM) in incomplete DMEM, followed by incubation with 25 μM Cf-labeled peptides or Dau-conjugates for 30 or 90 min. Subsequently, cell nuclei were stained with Hoechst 33342 solution (Thermo Fisher Scientific, Waltham, MA, USA) for 10 min (0.2 μM). After each step, cells were washed three times with PBS. Cells were fixed with 4% paraformaldehyde for 15 min (37 °C) and mounted on microscopy slides with Mowiol 4-88. For live cell imaging, U87 cells were seeded (45,000 cells/well) in complete DMEM cell culture medium 1 day prior to treatment in μ-Slide eight-well ibiTreat chambers (Ibidi GmbH, Gräfelfing, Germany). Lysosomes were stained with LysoTracker Red DND-99 (Invitrogen, Carlsbad, CA, USA) for 30 min (300 nM) in incomplete DMEM, followed by incubation with 25 μM Cf-labeled peptides for 30 or 90 min. Subsequently, cell nuclei were stained with Hoechst 33342 solution (0.2 μM) for 10 min. After each step, cells were washed three times with PBS. Imaging was performed on a Zeiss LSM 710 system (Carl Zeiss Microscopy GmbH, Jena, Germany) with a 40× oil immersion objective (40×/1.4 oil DIC M27). The following wavelengths were used for excitation and fluorescence emission detection: for Cf-peptides excitation at 488 nm, detection between 501 and 550 nm; for Dau-conjugates excitation at 458 nm, detection between 541 and 590 nm; for LysoTracker Deep Red excitation at 633 nm, detection between 643 and 797 nm; for LysoTracker Red DND-99 excitation at 543 nm, detection between 560 and 797 nm; for Hoechst 33342 excitation at 405 nm, detection between 410 and 587 nm. Different laser intensities were used in the case of compounds with low or high internalization to improve visualization and optimize the image quality; therefore, the CLSM observations cannot be considered as quantitative analysis but provide qualitative information about subcellular localization. Images were processed with ZEN 3.0 blue lite software (Carl Zeiss Microscopy GmbH).

Membrane Affinity Measurements on Lipid Monolayer as *ex vivo* BBB Model. The membrane affinity experiments were performed with a KSV MiniMicro (Finland) instrument at room temperature. The trough was equipped with two polyoxymethylene (POM) barriers while surface pressure was recorded tensiometrically with ±0.5 mN/m accuracy employing previously cleaned filter papers (Whatman Chr1) as Wilhelmy plates. DCM and methanol were used for the cleaning of the trough and barriers, respectively, before each measurement. Double distilled water used as a subphase was checked by its conductivity (<5 mS) and surface tension (>72.0 mN/m at 23 ± 0.5 °C) values. Brain extract polar lipid (BEPL, Avanti Polar Lipids Inc., USA) was applied in chloroform to form a monomolecular lipid layer on the double distilled water subphase in the Langmuir through to mimic the BBB lipid composition. The phospholipid composition (w/w%) of BEPL given by the supplier is 12.6 phosphatidylcholine, 33.1 phosphatidylethanolamine, 4.1 phosphatidylinositol, 18.5 phosphatidylserine, and 0.8 phosphatidic acid, whereas the other 30.9% are unknown. That means that the BEPL monolayer contains a significant amount (at least 23 wt %) of negatively charged lipid components. BEPL was dissolved in chloroform to a concentration of 0.2 mg/mL. After spreading of 50 μL lipid solution, the system was left for 10 min to allow the evaporation of the chloroform before the compression. Surface pressure−area isotherms were recorded two times before each penetration measurement. Compressing the lipid layer to the target pressure (25 or 30 mN/m) following a 5 min relaxation time, the aqueous solution of the Dau-peptide conjugate (concentration of 500 μM) was injected under the lipid monolayer to reach a 5 μM final concentration in the subphase. The changes of the surface pressure as a function of time were recorded for 30 min to detect the interaction/penetration of the Dau-peptide with/into the lipid layer. Three penetration measurements were performed in every case.

Penetration Ability Determination on TW Co-Culture with Noncontact HUVEC-U87 Monolayers as *in Vitro* BBB Model. TW system was tested in a number of preliminary experiments in order to optimize seeding procedure, pore size, and coating/non-coating for HUVECs. Cells, HUVEC and U87, were cultured and maintained as described in the Cell Cultures part of the Experimental Section. For barrier seeding, 24-well TW plates of 0.4 μm pore size were used (Corning, United Kingdom). Prior to use, TWs were soaked with PBS (growth area 0.385 cm^2). On day one, the apical side of the TW inserts was coated with 0.5% gelatin/PBS (v/v) and incubated for 30 min (37 °C, 5% CO$_2$). After incubation, gelatin solution was removed by careful aspiration and 150 μL of HUVEC suspension in complete MBCD medium ((3.0−6.0) × 10^5 cells) was pipetted onto the coated surface of the TW chamber and 500 μL MBCD medium added to the basolateral side. After the cells were cultured at 37 °C for 5−6 h, the apical medium was removed and replaced with fresh MBCD medium in order to avoid nonattached cells. Medium was changed also on day two, and HUVECs were grown up to confluence (which was checked prior to and after the experiments). At confluence, the endothelial cell monolayers were labeled with CellTracker Green (CMFDA (5-chloromethylfluorescein diacetate) dye, Invitrogen, C2925); for this purpose, CMFDA was used as 10 μM solution in serum free MBCD medium. After 30 min of incubation, the cells were washed with serum free MBCD. Cell nuclei of HUVEC monolayers were stained with Hoechst 33342 solution as described earlier. To capture the HUVEC layer, a ZEISS Axio Observer Inverse Imaging Platform (ZEISS) was used (equipped with Led3 470 blue, Led4 555 green; filter set: 25HE). On day three, medium was changed before the Dau-conjugate treatment, as starvation may affect protein expression in the endothelial cell monolayer. U87 cells (10^5 cells/well in complete DMEM) were seeded on day three prior to treatment on cover glasses (Assistent) inserted in the basolateral chambers of 24-well plates. Conjugates (Dau-Aoa-TKPPR, Dau-Aoa-SynB3, and Dau-Aoa-SynB3-TKPPR) were added to the HUVEC-containing apical side at 50 μM concentration, and the system was incubated for 45 min or 3 h (37 °C, 5% CO$_2$). After incubation, the TW chamber was removed. Cell nuclei of U87 cells forming the basolateral chamber were stained with Hoechst 33342; cells were fixed with 4% paraformaldehyde and mounted on microscopy slides with Mowiol 4-88 as described above. Fixed U87 cells were studied using confocal

microscopy (Zeiss LSM 710). As controls, U87 cells were treated without the presence of the TW inserts. The same wavelengths were used for excitation and fluorescence emission detection for Dau signal and Hoechst 33342 as described above. Laser intensity values were identical. Images were processed with ZEN 3.0 blue lite software. Cell groups were selected on the Dau (red) channel (seven groups in the case of Dau, 10−10 groups in the case of conjugates) with at least 3 cells/group. Selection was carried out manually in NIH ImageJ software based on the occurrence of cell nuclei (blue channel). Histograms and intensity values were obtained, and background corrected normalized fluorescence intensities (CNF) were calculated as follows: CNF = (ID − (A × MFB))/A, where ID is the integrated density, A is the area, and MFB is the mean fluorescence of the background. The obtained intensity in gray values corresponds to the intensity of a given pixel on a scale of 0−255. For visualization of histograms and normalized intensities, "violin plots" were used.[101]

In Vitro 3D Spheroid Formation and Confocal Microscopy of Spheroids. Molten agarose (2%, w/v in PBS) was pipetted into a silicon micromold 3D Petri dish (microtissues, Sigma-Aldrich, St. Louis, MO, USA, size L, 5 × 7 array, microwell diameter: 800 μm). After the agarose was gelled, the agarose microwell dish was transferred into a cell culture dish (polystyrene Petri dish, 35 × 10 mm, Sarstedt) and it was equilibrated with serum free DMEM cell culture medium (2 h, 37 °C). Cells were seeded into the agarose microwell dish, and 13 μL of cell suspension (10,000 cells/μL of complete DMEM) was used to fill the microwells under a stereo microscope (YJ-T3C, Ningbo Tianyu Optoelectronic Technology Co., Ltd., Beilun, Ningbo, China); this way, approximately 3500 cells were transferred in one well. Seeded cells were incubated in 2 mL of complete DMEM for 36 h (37 °C, 5% CO$_2$), while cell-to-cell adhesion drove the aggregation and formation of spheroids. To monitor the spheroids, bright-field images were captured using an Olympus CX41 microscope (Olympus Corporation, Hamburg, Germany). After 36 h of incubation, spheroids were washed two times with fresh serum free DMEM and they were treated in the microwells with the compounds at 25 μM concentration in 2 mL of serum free DMEM for 3 h (37 °C, 5% CO$_2$). After this, spheroids were washed two times with serum free DMEM and two times with PBS to remove the compounds that were not internalized. Nuclei were stained with Hoechst 33342 solution (0.2 μM) for 30 min. Spheroids were fixed with 4% paraformaldehyde for 15 min (37 °C). After each step, spheroids were washed three times with PBS and then harvested and transferred from the agarose microwells into μ-Slide eight-well uncoated chambers (Ibidi). Imaging was performed on a Zeiss LSM 710 system with a 10× dry objective (10×/0.45 M27). The same excitation and emission wavelengths were used as those for the 2D confocal microscopy imaging. Different laser intensities were used in the case of Dau and the Dau-conjugates to improve visualization and to optimize the image quality; therefore, the CLSM observations cannot be considered as quantitative analysis but provide qualitative information about the penetration ability. Z-Stack images were obtained by scanning the spheroids from the bottom of the spheroid with a 10 μm distance between each scanning plane. Images were processed with ZEN 3.0 blue lite software. Line scan and zonal scan analysis of section z5 with a depth of 50 μm was performed by NIH ImageJ software; for each sample, two parallel spheroids were analyzed (8 line scans/spheroid, n = 16 in total, three zones (periphery - zone 1, intermediate - zone 2, core - zone 3) per spheroid, n = 6 in total). Both analyses were carried out using grayscale images; a gray value corresponds to the intensity of a given pixel on a scale of 0 to 255. To average the intensity values from line scans of spheroid sections of slightly different size and shape, all line scan lengths were normalized to 1, yielding normalized diameter. Calculation of average and SEM of multiple curves was carried out using OriginPro 2018 software. In the case of zonal scans, spheroids were selected manually in ImageJ. Selection were scaled to obtain zones, and the scale factors are as follows: 1 for zone 1, 0.67 for zone 2, and 0.33 for zone 3. Intensity values were obtained by ImageJ, and background corrected normalized fluorescence intensities (CNF) were calculated as follows: CNF = (ID − (A × MFB))/A, where ID is the integrated density, A is the area, and MFB is the mean fluorescence of the background. The normalized

intensities were standardized as the proportion of the mean intensity in the peripheries (0–100%) and plotted using OriginPro 2018. For statistical analysis, see Figure S32 and Table S7.

Statistical Analysis. Due to the variance heterogeneity of the studied groups (i.e., conjugates) and non-normal distribution (based on the performed Bartlett's test and Shapiro–Wilk normality tests, respectively), Kruskal–Wallis nonparametric tests were used to compare the effects of the conjugates on cellular uptake.[102] In the case of a significant treatment effect (a p-value <0.05 was considered as significant), the differences between the conjugates were tested by pairwise multiple comparisons following Dunn's method. To control the family-wise error rate, p-values of the post hoc tests were adjusted by Holm's method. For comparison of the cytostatic effect of Dau or Sal3-conjugated peptide derivatives with the corresponding drug alone, Dunnett's post hoc test with Holm correction was used. ANOVA was used to analyze the treatment effect on the BBB model TW system. All statistical analyses were performed using R version 3.6.1.[103] For multiple comparisons package, "PMCMR" was used.[104]

ASSOCIATED CONTENT

Supporting Information

The Supporting Information is available free of charge at https://pubs.acs.org/doi/10.1021/acs.jmedchem.0c01399.

Monitoring of the conjugation reactions, characterization of TMZA, characterization of the compounds, analytical RP-HPLC chromatograms of lead compounds, stability study of the conjugates, digestion profile of conjugates in rat liver lysosomal homogenate and LC-MS analysis, *in vitro* cytostatic and cytotoxic activity, determination of the pH dependence of the fluorescence intensity, cellular uptake studies, confocal microscopy studies, in vitro BBB model studies, and spheroid studies (PDF)

Molecular formula string (CSV)

Molecular formula string (XLSX)

AUTHOR INFORMATION

Corresponding Author

Szilvia Bősze − *Eötvös Loránd Research Network, Research Group of Peptide Chemistry, Eötvös Loránd University, H-1117 Budapest, Hungary;* orcid.org/0000-0001-9555-699X; Phone: +36-372-2500; Email: bosze@elte.hu; Fax: +36-372-26-20

Authors

Zsuzsa Baranyai − *Eötvös Loránd Research Network, Research Group of Peptide Chemistry, Eötvös Loránd University, H-1117 Budapest, Hungary;* orcid.org/0000-0002-2174-6747

Beáta Biri-Kovács − *Eötvös Loránd Research Network, Research Group of Peptide Chemistry and Institute of Chemistry, Eötvös Loránd University, H-1117 Budapest, Hungary;* orcid.org/0000-0001-5803-9969

Martin Krátký − *Department of Organic and Bioorganic Chemistry, Faculty of Pharmacy in Hradec Králové, Charles University, 500 05 Hradec Králové, Czech Republic*

Bálint Szeder − *Institute of Enzymology, Research Centre for Natural Sciences, H-1117 Budapest, Hungary*

Márta L. Debreczeni − *3rd Department of Medicine Research Laboratory, Semmelweis University, H-1125 Budapest, Hungary*

Johanna Budai − *Eötvös Loránd Research Network, Research Group of Peptide Chemistry, Eötvös Loránd University, H-1117 Budapest, Hungary*

Bence Kovács − *Centre for Ecological Research, Institute of Ecology and Botany, H-2163 Vácrátót, Hungary*

Lilla Horváth − *Eötvös Loránd Research Network, Research Group of Peptide Chemistry, Eötvös Loránd University, H-1117 Budapest, Hungary*

Edit Pári − *Laboratory of Interfaces and Nanostructures, Institute of Chemistry, Eötvös Loránd University, H-1117 Budapest, Hungary*

Zsuzsanna Németh − *3rd Department of Medicine Research Laboratory, Semmelweis University, H-1125 Budapest, Hungary*

László Cervenak − *3rd Department of Medicine Research Laboratory, Semmelweis University, H-1125 Budapest, Hungary*

Ferenc Zsila − *Institute of Materials and Environmental Chemistry, Research Centre for Natural Sciences, H-1117 Budapest, Hungary;* orcid.org/0000-0002-4853-2810

Előd Méhes − *Department of Biological Physics, Institute of Physics, Eötvös Loránd University, H-1117 Budapest, Hungary*

Éva Kiss − *Laboratory of Interfaces and Nanostructures, Institute of Chemistry, Eötvös Loránd University, H-1117 Budapest, Hungary*

Jarmila Vinšová − *Department of Organic and Bioorganic Chemistry, Faculty of Pharmacy in Hradec Králové, Charles University, 500 05 Hradec Králové, Czech Republic*

Complete contact information is available at:
https://pubs.acs.org/10.1021/acs.jmedchem.0c01399

Author Contributions

The manuscript was written through contributions of all authors. All authors have given approval to the final version of the manuscript.

Notes

The authors declare no competing financial interest.

ACKNOWLEDGMENTS

◼ ABBREVIATIONS USED

SynB3, RRLSYSRRRF; GFLG-SynB3, GFLG-RRLSYSRRRF; SynB3K, RRLSYSRRRFK; SynB3K(dec), RRLSYSRRRFK-(decanoyl); T5, TKPKG; GFLG-T5, GFLG-TKPKG; T5(4-dec), TKPK(decanoyl)G; TKPPG-OT10, TKPPG-TKPKG-TKPKG; H-, free N-terminal; Ac-, acetylated N-terminal; Cf-, 5(6)-carboxyfluorescein on the N-terminal; Sal3-Aoa-, salicylanilide conjugated by an oxime bond to the N-terminal of the peptide; Dau-Aoa-, daunomycin conjugated by an oxime bond to the N-terminal of the peptide; TMZ-, temozolomide conjugated by an amide bond to the N-terminal of the peptide; UC_{50}, compound concentration where the rate of cells displaying fluorescence reaches 50%; BEPL, brain extract polar lipid; BBB, blood–brain barrier; TW, Transwell

◼ REFERENCES

(1) Weller, M.; Wick, W.; Aldape, K.; Brada, M.; Berger, M.; Pfister, S. M.; Nishikawa, R.; Rosenthal, M.; Wen, P. Y.; Stupp, R.; Reifenberger, G. Glioma. *Nat. Rev. Dis Primers* **2015**, *1*, 15017.

(2) Stupp, R.; Taillibert, S.; Kanner, A.; Read, W.; Steinberg, D.; Lhermitte, B.; Toms, S.; Idbaih, A.; Ahluwalia, M. S.; Fink, K.; Di Meco, F.; Lieberman, F.; Zhu, J. J.; Stragliotto, G.; Tran, D.; Brem, S.; Hottinger, A.; Kirson, E. D.; Lavy-Shahaf, G.; Weinberg, U.; Kim, C. Y.; Paek, S. H.; Nicholas, G.; Bruna, J.; Hirte, H.; Weller, M.; Palti, Y.; Hegi, M. E.; Ram, Z. Effect of Tumor-Treating Fields Plus Maintenance Temozolomide vs Maintenance Temozolomide Alone on Survival in Patients with Glioblastoma: A Randomized Clinical Trial. *JAMA* **2017**, *318*, 2306–2316.

(3) Shergalis, A.; Bankhead, A., 3rd; Luesakul, U.; Muangsin, N.; Neamati, N. Current Challenges and Opportunities in Treating Glioblastoma. *Pharmacol. Rev.* **2018**, *70*, 412–445.

(4) Robertson, F. L.; Marques-Torrejon, M. A.; Morrison, G. M.; Pollard, S. M. Experimental Models and Tools to Tackle Glioblastoma. *Dis. Models Mech.* **2019**, *12*, dmm040386.

(5) Vollmann-Zwerenz, A.; Leidgens, V.; Feliciello, G.; Klein, C. A.; Hau, P. Tumor Cell Invasion in Glioblastoma. *Int. J. Mol. Sci.* **2020**, *21*, 1932.

(6) Liebelt, B. D.; Shingu, T.; Zhou, X.; Ren, J.; Shin, S. A.; Hu, J. Glioma Stem Cells: Signaling, Microenvironment, and Therapy. *Stem Cells Int.* **2016**, *2016*, 7849890.

(7) Abbott, N. J.; Patabendige, A. A.; Dolman, D. E.; Yusof, S. R.; Begley, D. J. Structure and Function of the Blood-Brain Barrier. *Neurobiol. Dis.* **2010**, *37*, 13–25.

(8) van Tellingen, O.; Yetkin-Arik, B.; de Gooijer, M. C.; Wesseling, P.; Wurdinger, T.; de Vries, H. E. Overcoming the Blood-Brain Tumor Barrier for Effective Glioblastoma Treatment. *Drug Resist. Updates* **2015**, *19*, 1–12.

(9) Sarkaria, J. N.; Hu, L. S.; Parney, I. F.; Pafundi, D. H.; Brinkmann, D. H.; Laack, N. N.; Giannini, C.; Burns, T. C.; Kizilbash, S. H.; Laramy, J. K.; Swanson, K. R.; Kaufmann, T. J.; Brown, P. D.; Agar, N. Y. R.; Galanis, E.; Buckner, J. C.; Elmquist, W. F. Is the Blood-Brain Barrier Really Disrupted in All Glioblastomas? A Critical Assessment of Existing Clinical Data. *Neuro Oncol* **2018**, *20*, 184–191.

(10) Lu, C. T.; Zhao, Y. Z.; Wong, H. L.; Cai, J.; Peng, L.; Tian, X. Q. Current Approaches to Enhance CNS Delivery of Drugs across the Brain Barriers. *Int. J. Nanomed.* **2014**, *9*, 2241–2257.

(11) Ghosh, D.; Peng, X.; Leal, J.; Mohanty, R. Peptides as Drug Delivery Vehicles across Biological Barriers. *J. Pharm. Invest.* **2018**, *48*, 89–111.

(12) Pardridge, W. M. Molecular Trojan Horses for Blood-Brain Barrier Drug Delivery. *Curr. Opin. Pharmacol.* **2006**, *6*, 494–500.

(13) Regberg, J.; Srimanee, A.; Langel, U. Applications of Cell-Penetrating Peptides for Tumor Targeting and Future Cancer Therapies. *Pharmaceuticals* **2012**, *5*, 991–1007.

(14) Oller-Salvia, B.; Sanchez-Navarro, M.; Giralt, E.; Teixido, M. Blood-Brain Barrier Shuttle Peptides: An Emerging Paradigm for Brain Delivery. *Chem. Soc. Rev.* **2016**, *45*, 4690–4707.

(15) Rousselle, C.; Clair, P.; Lefauconnier, J. M.; Kaczorek, M.; Scherrmann, J. M.; Temsamani, J. New Advances in the Transport of Doxorubicin through the Blood-Brain Barrier by a Peptide Vector-Mediated Strategy. *Mol. Pharmacol.* **2000**, *57*, 679–686.

(16) Rousselle, C.; Smirnova, M.; Clair, P.; Lefauconnier, J. M.; Chavanieu, A.; Calas, B.; Scherrmann, J. M.; Temsamani, J. Enhanced Delivery of Doxorubicin into the Brain via a Peptide-Vector-Mediated Strategy: Saturation Kinetics and Specificity. *J. Pharmacol. Exp. Ther.* **2001**, *296*, 124–131.

(17) Kokryakov, V. N.; Harwig, S. S.; Panyutich, E. A.; Shevchenko, A. A.; Aleshina, G. M.; Shamova, O. V.; Korneva, H. A.; Lehrer, R. I. Protegrins: Leukocyte Antimicrobial Peptides that Combine Features of Corticostatic Defensins and Tachyplesins. *FEBS Lett.* **1993**, *327*, 231–236.

(18) Aumelas, A.; Mangoni, M.; Roumestand, C.; Chiche, L.; Despaux, E.; Grassy, G.; Calas, B.; Chavanieu, A. Synthesis and Solution Structure of the Antimicrobial Peptide Protegrin-1. *Eur. J. Biochem.* **1996**, *237*, 575–583.

(19) Bolintineanu, D. S.; Sayyed-Ahmad, A.; Davis, H. T.; Kaznessis, Y. N. Poisson-Nernst-Planck Models of Nonequilibrium Ion Electrodiffusion through a Protegrin Transmembrane Pore. *PLoS Comput. Biol.* **2009**, *5*, e1000277.

(20) Drin, G.; Rousselle, C.; Scherrmann, J. M.; Rees, A. R.; Temsamani, J. Peptide Delivery to the Brain via Adsorptive-Mediated Endocytosis: Advances with SynB Vectors. *AAPS PharmSci* **2002**, *4*, E26.

(21) Drin, G.; Cottin, S.; Blanc, E.; Rees, A. R.; Temsamani, J. Studies on the Internalization Mechanism of Cationic Cell-Penetrating Peptides. *J. Biol. Chem.* **2003**, *278*, 31192–31201.

(22) Herve, F.; Ghinea, N.; Scherrmann, J. M. CNS Delivery via Adsorptive Transcytosis. *AAPS J.* **2008**, *10*, 455–472.

(23) Mazel, M.; Clair, P.; Rousselle, C.; Vidal, P.; Scherrmann, J. M.; Mathieu, D.; Temsamani, J. Doxorubicin-Peptide Conjugates Overcome Multidrug Resistance. *Anti-Cancer Drugs* **2001**, *12*, 107–116.

(24) Blanc, E.; Bonnafous, C.; Merida, P.; Cisternino, S.; Clair, P.; Scherrmann, J. M.; Temsamani, J. Peptide-Vector Strategy Bypasses P-Glycoprotein Efflux, and Enhances Brain Transport and Solubility of Paclitaxel. *Anti-Cancer Drugs* **2004**, *15*, 947–954.

(25) Rousselle, C.; Clair, P.; Temsamani, J.; Scherrmann, J. M. Improved Brain Delivery of Benzylpenicillin with a Peptide-Vector-Mediated Strategy. *J. Drug Target* **2002**, *10*, 309–315.

(26) Rousselle, C.; Clair, P.; Smirnova, M.; Kolesnikov, Y.; Pasternak, G. W.; Gac-Breton, S.; Rees, A. R.; Scherrmann, J. M.; Temsamani, J. Improved Brain Uptake and Pharmacological Activity of Dalargin Using a Peptide-Vector-Mediated Strategy. *J. Pharmacol. Exp. Ther.* **2003**, *306*, 371–376.

(27) Temsamani, J.; Bonnafous, C.; Rousselle, C.; Fraisse, Y.; Clair, P.; Granier, L. A.; Rees, A. R.; Kaczorek, M.; Scherrmann, J. M. Improved Brain Uptake and Pharmacological Activity Profile of Morphine-6-Glucuronide Using a Peptide Vector-Mediated Strategy. *J. Pharmacol. Exp. Ther.* **2005**, *313*, 712–719.

(28) Adenot, M.; Merida, P.; Lahana, R. Applications of a Blood-Brain Barrier Technology Platform to Predict CNS Penetration of Various Chemotherapeutic Agents. 2. Cationic Peptide Vectors for Brain Delivery. *Chemotherapy* **2007**, *53*, 73–76.

(29) Castex, C.; Merida, P.; Blanc, E.; Clair, P.; Rees, A. R.; Temsamani, J. 2-Pyrrolinodoxorubicin and Its Peptide-Vectorized Form Bypass Multidrug Resistance. *Anti-Cancer Drugs* **2004**, *15*, 609–617.

(30) Liu, H.; Zhang, W.; Ma, L.; Fan, L.; Gao, F.; Ni, J.; Wang, R. The Improved Blood-Brain Barrier Permeability of Endomorphin-1 Using the Cell-Penetrating Peptide SynB3 with Three Different Linkages. *Int. J. Pharm.* **2014**, *476*, 1–8.

(31) Tian, X. H.; Wei, F.; Wang, T. X.; Wang, P.; Lin, X. N.; Wang, J.; Wang, D.; Ren, L. In Vitro and in Vivo Studies on Gelatin-Siloxane Nanoparticles Conjugated with SynB Peptide to Increase Drug Delivery to the Brain. *Int. J. Nanomed.* **2012**, *7*, 1031–1041.

(32) Stalmans, S.; Bracke, N.; Wynendaele, E.; Gevaert, B.; Peremans, K.; Burvenich, C.; Polis, I.; De Spiegeleer, B. Cell-Penetrating Peptides

Selectively Cross the Blood-Brain Barrier In Vivo. *PLoS One* **2015**, *10*, No. e0139652.

(33) Leng, Q.; Woodle, M. C.; Mixson, A. J. NRP1 Transport of Cancer Therapeutics Mediated by Tumor-Penetrating Peptides. *Drugs Future* **2017**, *42*, 95−104.

(34) Wang, Y.; Cao, Y.; Mangalam, A. K.; Guo, Y.; LaFrance-Corey, R. G.; Gamez, J. D.; Atanga, P. A.; Clarkson, B. D.; Zhang, Y.; Wang, E.; Angom, R. S.; Dutta, K.; Ji, B.; Pirko, I.; Lucchinetti, C. F.; Howe, C. L.; Mukhopadhyay, D. Neuropilin-1 Modulates Interferon-Gamma-Stimulated Signaling in Brain Microvascular Endothelial Cells. *J. Cell Sci.* **2016**, *129*, 3911−3921.

(35) Chen, L.; Shi, Y.; Qiu, R. Neuropilin-1 (NRP-1), a Novel Molecular Target of Glioma. *J. Nanosci. Nanotechnol.* **2016**, *16*, 6657−6666.

(36) Pellet-Many, C.; Frankel, P.; Jia, H.; Zachary, I. Neuropilins: Structure, Function and Role in Disease. *Biochem. J.* **2008**, *411*, 211−226.

(37) Teesalu, T.; Sugahara, K. N.; Kotamraju, V. R.; Ruoslahti, E. C-End Rule Peptides Mediate Neuropilin-1-Dependent Cell, Vascular, and Tissue Penetration. *Proc. Natl. Acad. Sci. U. S. A.* **2009**, *106*, 16157−16162.

(38) Sugahara, K. N.; Teesalu, T.; Karmali, P. P.; Kotamraju, V. R.; Agemy, L.; Girard, O. M.; Hanahan, D.; Mattrey, R. F.; Ruoslahti, E. Tissue-Penetrating Delivery of Compounds and Nanoparticles into Tumors. *Cancer Cell* **2009**, *16*, 510−520.

(39) Teesalu, T.; Sugahara, K. N.; Ruoslahti, E. Tumor-Penetrating Peptides. *Front. Oncol.* **2013**, *3*, 216.

(40) Ruoslahti, E. Tumor Penetrating Peptides for Improved Drug Delivery. *Adv. Drug Delivery Rev.* **2017**, *110−111*, 3−12.

(41) Pang, H. B.; Braun, G. B.; Friman, T.; Aza-Blanc, P.; Ruidiaz, M. E.; Sugahara, K. N.; Teesalu, T.; Ruoslahti, E. An Endocytosis Pathway Initiated through Neuropilin-1 and Regulated by Nutrient Availability. *Nat. Commun.* **2014**, *5*, 4904.

(42) Siemion, I. Z.; Kluczyk, A. Tuftsin: On the 30-Year Anniversary of Victor Najjar's Discovery. *Peptides* **1999**, *20*, 645−674.

(43) von Wronski, M. A.; Raju, N.; Pillai, R.; Bogdan, N. J.; Marinelli, E. R.; Nanjappan, P.; Ramalingam, K.; Arunachalam, T.; Eaton, S.; Linder, K. E.; Yan, F.; Pochon, S.; Tweedle, M. F.; Nunn, A. D. Tuftsin Binds Neuropilin-1 through a Sequence Similar to That Encoded by Exon 8 of Vascular Endothelial Growth Factor. *J. Biol. Chem.* **2006**, *281*, 5702−5710.

(44) Nissen, J. C.; Selwood, D. L.; Tsirka, S. E. Tuftsin Signals through Its Receptor Neuropilin-1 via the Transforming Growth Factor Beta Pathway. *J. Neurochem.* **2013**, *127*, 394−402.

(45) Bump, N. J.; Lee, J.; Wleklik, M.; Reichler, J.; Najjar, V. A. Isolation and Subunit Composition of Tuftsin Receptor. *Proc. Natl. Acad. Sci. U. S. A.* **1986**, *83*, 7187−7191.

(46) Mezo, G.; Kalaszi, A.; Remenyi, J.; Majer, Z.; Hilbert, A.; Lang, O.; Kohidai, L.; Barna, K.; Gaal, D.; Hudecz, F. Synthesis, Conformation, and Immunoreactivity of New Carrier Molecules Based on Repeated Tuftsin-Like Sequence. *Biopolymers* **2004**, *73*, 645−656.

(47) Bai, K. B.; Lang, O.; Orban, E.; Szabo, R.; Kohidai, L.; Hudecz, F.; Mezo, G. Design, Synthesis, and In Vitro Activity of Novel Drug Delivery Systems Containing Tuftsin Derivatives and Methotrexate. *Bioconjugate Chem.* **2008**, *19*, 2260−2269.

(48) Horvati, K.; Bacsa, B.; Szabo, N.; David, S.; Mezo, G.; Grolmusz, V.; Vertessy, B.; Hudecz, F.; Bosze, S. Enhanced Cellular Uptake of a New, In Silico Identified Antitubercular Candidate by Peptide Conjugation. *Bioconjugate Chem.* **2012**, *23*, 900−907.

(49) Abraham, A.; Baranyai, Z.; Gyulai, G.; Pari, E.; Horvati, K.; Bosze, S.; Kiss, E. Comparative Analysis of New Peptide Conjugates of Antitubercular Drug Candidates-Model Membrane and In Vitro Studies. *Colloids Surf., B* **2016**, *147*, 106−115.

(50) Baranyai, Z.; Kratky, M.; Vosatka, R.; Szabo, E.; Senoner, Z.; David, S.; Stolarikova, J.; Vinsova, J.; Bosze, S. In Vitro Biological Evaluation of New Antimycobacterial Salicylanilide-Tuftsin Conjugates. *Eur. J. Med. Chem.* **2017**, *133*, 152−173.

(51) Kratky, M.; Vinsova, J. Salicylanilide Ester Prodrugs as Potential Antimicrobial Agents–a Review. *Curr. Pharm. Des.* **2011**, *17*, 3494−3505.

(52) Li, Y.; Li, P. K.; Roberts, M. J.; Arend, R. C.; Samant, R. S.; Buchsbaum, D. J. Multi-Targeted Therapy of Cancer by Niclosamide: A New Application for an Old Drug. *Cancer Lett.* **2014**, *349*, 8−14.

(53) Chen, W.; Mook, R. A., Jr.; Premont, R. T.; Wang, J. Niclosamide: Beyond an Antihelminthic Drug. *Cell. Signalling* **2018**, *41*, 89−96.

(54) Pan, J. X.; Ding, K.; Wang, C. Y. Niclosamide, an Old Antihelminthic Agent, Demonstrates Antitumor Activity by Blocking Multiple Signaling Pathways of Cancer Stem Cells. *Aizheng* **2012**, *31*, 178−184.

(55) Wieland, A.; Trageser, D.; Gogolok, S.; Reinartz, R.; Hofer, H.; Keller, M.; Leinhaas, A.; Schelle, R.; Normann, S.; Klaas, L.; Waha, A.; Koch, P.; Fimmers, R.; Pietsch, T.; Yachnis, A. T.; Pincus, D. W.; Steindler, D. A.; Brustle, O.; Simon, M.; Glas, M.; Scheffler, B. Anticancer Effects of Niclosamide in Human Glioblastoma. *Clin. Cancer Res.* **2013**, *19*, 4124−4136.

(56) Cheng, B.; Morales, L. D.; Zhang, Y.; Mito, S.; Tsin, A. Niclosamide Induces Protein Ubiquitination and Inhibits Multiple Pro-Survival Signaling Pathways in the Human Glioblastoma U-87 MG Cell Line. *PLoS One* **2017**, *12*, No. e0184324.

(57) Myrberg, H.; Zhang, L.; Mae, M.; Langel, U. Design of a Tumor-Homing Cell-Penetrating Peptide. *Bioconjugate Chem.* **2008**, *19*, 70−75.

(58) Ren, Y.; Cheung, H. W.; von Maltzhan, G.; Agrawal, A.; Cowley, G. S.; Weir, B. A.; Boehm, J. S.; Tamayo, P.; Karst, A. M.; Liu, J. F.; Hirsch, M. S.; Mesirov, J. P.; Drapkin, R.; Root, D. E.; Lo, J.; Fogal, V.; Ruoslahti, E.; Hahn, W. C.; Bhatia, S. N. Targeted Tumor-Penetrating siRNA Nanocomplexes for Credentialing the Ovarian Cancer Oncogene Id4. *Sci. Transl. Med.* **2012**, *4*, 147ra112.

(59) Crisp, J. L.; Savariar, E. N.; Glasgow, H. L.; Ellies, L. G.; Whitney, M. A.; Tsien, R. Y. Dual Targeting of Integrin Alphavbeta3 and Matrix Metalloproteinase-2 for Optical Imaging of Tumors and Chemo-therapeutic Delivery. *Mol. Cancer Ther.* **2014**, *13*, 1514−1525.

(60) Liu, Y.; Ran, R.; Chen, J.; Kuang, Q.; Tang, J.; Mei, L.; Zhang, Q.; Gao, H.; Zhang, Z.; He, Q. Paclitaxel Loaded Liposomes Decorated with a Multifunctional Tandem Peptide for Glioma Targeting. *Biomaterials* **2014**, *35*, 4835−4847.

(61) Feni, L.; Parente, S.; Robert, C.; Gazzola, S.; Arosio, D.; Piarulli, U.; Neundorf, I. Kiss and Run: Promoting Effective and Targeted Cellular Uptake of a Drug Delivery Vehicle Composed of an Integrin-Targeting Diketopiperazine Peptidomimetic and a Cell-Penetrating Peptide. *Bioconjugate Chem.* **2019**, *30*, 2011−2022.

(62) Agarwala, S. S.; Kirkwood, J. M. Temozolomide, a Novel Alkylating Agent with Activity in the Central Nervous System, May Improve the Treatment of Advanced Metastatic Melanoma. *Oncologist* **2000**, *5*, 144−151.

(63) Baranyai, Z.; Kratky, M.; Vinsova, J.; Szabo, N.; Senoner, Z.; Horvati, K.; Stolarikova, J.; David, S.; Bosze, S. Combating Highly Resistant Emerging Pathogen Mycobacterium Abscessus and Myco-bacterium Tuberculosis with Novel Salicylanilide Esters and Carbamates. *Eur. J. Med. Chem.* **2015**, *101*, 692−704.

(64) Futaki, S.; Ohashi, W.; Suzuki, T.; Niwa, M.; Tanaka, S.; Ueda, K.; Harashima, H.; Sugiura, Y. Stearylated Arginine-Rich Peptides: A New Class of Transfection Systems. *Bioconjugate Chem.* **2001**, *12*, 1005−1011.

(65) Ezzat, K.; Andaloussi, S. E.; Zaghloul, E. M.; Lehto, T.; Lindberg, S.; Moreno, P. M.; Viola, J. R.; Magdy, T.; Abdo, R.; Guterstam, P.; Sillard, R.; Hammond, S. M.; Wood, M. J.; Arzumanov, A. A.; Gait, M. J.; Smith, C. I.; Hallbrink, M.; Langel, U. Pepfect 14, a Novel Cell-Penetrating Peptide for Oligonucleotide Delivery in Solution and as Solid Formulation. *Nucleic Acids Res.* **2011**, *39*, 5284−5298.

(66) Kiss, E.; Schnoller, D.; Pribranska, K.; Hill, K.; Penzes, C. B.; Horvati, K.; Bosze, S. Nanoencapsulation of Antitubercular Drug Isoniazid and Its Lipopeptide Conjugate. *J. Dispersion Sci. Technol.* **2011**, *32*, 1728−1734.

(67) Shao, J.; Tam, J. P. Unprotected Peptides as Building Blocks for the Synthesis of Peptide Dendrimers with Oxime, Hydrazone, and Thiazolidine Linkages. *J. Am. Chem. Soc.* **1995**, *117*, 3893–3899.

(68) Naqvi, S. A.; Matzow, T.; Finucane, C.; Nagra, S. A.; Ishfaq, M. M.; Mather, S. J.; Sosabowski, J. Insertion of a Lysosomal Enzyme Cleavage Site into the Sequence of a Radiolabeled Neuropeptide Influences Cell Trafficking In Vitro and In Vivo. *Cancer Biother. Radiopharm.* **2010**, *25*, 89–95.

(69) Vrettos, E. I.; Mezo, G.; Tzakos, A. G. On the Design Principles of Peptide-Drug Conjugates for Targeted Drug Delivery to the Malignant Tumor Site. *Beilstein J. Org. Chem.* **2018**, *14*, 930–954.

(70) Arrowsmith, J.; Jennings, S. A.; Clark, A. S.; Stevens, M. F. Antitumor Imidazotetrazines. 41. Conjugation of the Antitumor Agents Mitozolomide and Temozolomide to Peptides and Lexitropsins Bearing DNA Major and Minor Groove-Binding Structural Motifs. *J. Med. Chem.* **2002**, *45*, 5458–5470.

(71) Skinner, M.; Ward, S. M.; Emrick, T. Versatile Synthesis of Polymer-Temozolomide Conjugates. *ACS Macro Lett.* **2017**, *6*, 215–218.

(72) Toniolo, C. F. F.; Woody, R. W. Electronic Circular Dichroism of Peptides. In *Comprehensive Chiroptical Spectroscopy: Applications in Stereochemical Analysis of Synthetic Compounds, Natural Products, and Biomolecules*; Berova, N., Polavarapu, P. L., Nakanishi, K., Woody, R. W., Eds.; Wiley: 2012; Vol. 2, pp 499–544.

(73) Woody, R. W. Circular Dichroism Spectrum of Peptides in the Poly(Pro)II Conformation. *J. Am. Chem. Soc.* **2009**, *131*, 8234–8245.

(74) Bosze, S.; Zsila, F.; Biri-Kovacs, B.; Szeder, B.; Majer, Z.; Hudecz, F.; Uray, K. Tailoring Uptake Efficacy of HSV-1 gD Derived Carrier Peptides. *Biomolecules* **2020**, *10*, 721.

(75) Vincenzi, M.; Mercurio, F. A.; Leone, M. About TFE: Old and New Findings. *Curr. Protein Pept. Sci.* **2019**, *20*, 425–451.

(76) Yan, J.; Liang, X.; Liu, C.; Cheng, Y.; Zhou, L.; Wang, K.; Zhao, L. Influence of Proline Substitution on the Bioactivity of Mammalian-Derived Antimicrobial Peptide NK-2. *Probiotics Antimicrob. Proteins* **2018**, *10*, 118–127.

(77) Imai, K.; Mitaku, S. Mechanisms of Secondary Structure Breakers in Soluble Proteins. *Biophysics (Biophys. Soc. Jpn.)* **2005**, *1*, 55–65.

(78) Mindell, J. A. Lysosomal Acidification Mechanisms. *Annu. Rev. Physiol.* **2012**, *74*, 69–86.

(79) Orban, E.; Mezo, G.; Schlage, P.; Csik, G.; Kulic, Z.; Ansorge, P.; Fellinger, E.; Mőller, H. M.; Manea, M. In Vitro Degradation and Antitumor Activity of Oxime Bond-Linked Daunorubicin-GnRH-III Bioconjugates and DNA-Binding Properties of Daunorubicin-Amino Acid Metabolites. *Amino Acids* **2011**, *41*, 469–483.

(80) Price, J. E.; Polyzos, A.; Zhang, R. D.; Daniels, L. M. Tumorigenicity and Metastasis of Human Breast Carcinoma Cell Lines in Nude Mice. *Cancer Res.* **1990**, *50*, 717–721.

(81) Cailleau, R.; Olive, M.; Cruciger, Q. V. Long-Term Human Breast Carcinoma Cell Lines of Metastatic Origin: Preliminary Characterization. *In Vitro* **1978**, *14*, 911–915.

(82) Korch, C.; Hall, E. M.; Dirks, W. G.; Ewing, M.; Faries, M.; Varella-Garcia, M.; Robinson, S.; Storts, D.; Turner, J. A.; Wang, Y.; Burnett, E. C.; Healy, L.; Kniss, D.; Neve, R. M.; Nims, R. W.; Reid, Y. A.; Robinson, W. A.; Capes-Davis, A. Authentication of M14 Melanoma Cell Line Proves Misidentification of MDA-MB-435 Breast Cancer Cell Line. *Int. J. Cancer* **2018**, *142*, 561–572.

(83) Randelovic, I.; Schuster, S.; Kapuvari, B.; Fossati, G.; Steinkuhler, C.; Mezo, G.; Tovari, J. Improved in Vivo Anti-Tumor and Anti-Metastatic Effect of GnRH-III-Daunorubicin Analogs on Colorectal and Breast Carcinoma Bearing Mice. *Int. J. Mol. Sci.* **2019**, *20*, 4763.

(84) Tripodi, A. A. P.; Randelovic, I.; Biri-Kovacs, B.; Szeder, B.; Mezo, G.; Tovari, J. In Vivo Tumor Growth Inhibition and Antiangiogenic Effect of Cyclic NGR Peptide-Daunorubicin Conjugates Developed for Targeted Drug Delivery. *Pathol. Oncol. Res.* **2020**, *26*, 1879–1892.

(85) Dokus, L. E.; Lajko, E.; Randelovic, I.; Mezo, D.; Schlosser, G.; Kohidai, L.; Tovari, J.; Mezo, G. Phage Display-Based Homing Peptide-Daunomycin Conjugates for Selective Drug Targeting to Panc-1 Pancreatic Cancer. *Pharmaceutics* **2020**, *12*, 576.

(86) Casey, J. R.; Grinstein, S.; Orlowski, J. Sensors and Regulators of Intracellular Ph. *Nat. Rev. Mol. Cell Biol.* **2010**, *11*, 50–61.

(87) Biri-Kovacs, B.; Adorjan, A.; Szabo, I.; Szeder, B.; Bosze, S.; Mezo, G. Structure-Activity Relationship of HER2 Receptor Targeting Peptide and Its Derivatives in Targeted Tumor Therapy. *Biomolecules* **2020**, *10*, 183.

(88) Illien, F.; Rodriguez, N.; Amoura, M.; Joliot, A.; Pallerla, M.; Cribier, S.; Burlina, F.; Sagan, S. Quantitative Fluorescence Spectroscopy and Flow Cytometry Analyses of Cell-Penetrating Peptides Internalization Pathways: Optimization, Pitfalls, Comparison with Mass Spectrometry Quantification. *Sci. Rep.* **2016**, *6*, 36938.

(89) Kiss, E.; Gyulai, G.; Pari, E.; Horvati, K.; Bosze, S. Membrane Affinity and Fluorescent Labelling: Comparative Study of Monolayer Interaction, Cellular Uptake and Cytotoxicity Profile of Carboxy-fluorescein-Conjugated Cationic Peptides. *Amino Acids* **2018**, *50*, 1557–1571.

(90) Langel, Ü. *CPP, Cell-Penetrating Peptides*, 1st ed.; Springer: Singapore, 2019; pp XII, 470. DOI: 10.1007/978-981-13-8747-0.

(91) Birch, D.; Christensen, M. V.; Staerk, D.; Franzyk, H.; Nielsen, H. M. Fluorophore Labeling of a Cell-Penetrating Peptide Induces Differential Effects on Its Cellular Distribution and Affects Cell Viability. *Biochim. Biophys. Acta, Biomembr.* **2017**, *1859*, 2483–2494.

(92) Mendez-Ardoy, A.; Lostale-Seijo, I.; Montenegro, J. Where in the Cell Is Our Cargo? Methods Currently Used to Study Intracellular Cytosolic Localisation. *ChemBioChem* **2019**, *20*, 488–498.

(93) Sani, M. A.; Gehman, J. D.; Separovic, F. Lipid Matrix Plays a Role in Abeta Fibril Kinetics and Morphology. *FEBS Lett.* **2011**, *585*, 749–754.

(94) Sandrino, B.; Jochelavicius, K.; Volpati, D.; Barbosa, S. C.; Nobre, T. M.; Oliveira, O. N., Jr The Prion Fragment Prp106–127 Adopts a Secondary Structure Typical of Aggregated Fibrils in Langmuir Monolayers of Brain Lipid Extract. *Chem. Phys. Lipids* **2020**, *230*, 104930.

(95) Pari, E.; Horvati, K.; Bosze, S.; Biri-Kovacs, B.; Szeder, B.; Zsila, F.; Kiss, E. Drug Conjugation Induced Modulation of Structural and Membrane Interaction Features of Cationic Cell-Permeable Peptides. *Int. J. Mol. Sci.* **2020**, *21*, 2197.

(96) Bicker, J.; Alves, G.; Fortuna, A.; Falcão, A. Blood-Brain Barrier Models and Their Relevance for a Successful Development of CNS Drug Delivery Systems: A Review. *Eur. J. Pharm. Biopharm.* **2014**, *87*, 409–432.

(97) Yamada, K. M.; Cukierman, E. Modeling Tissue Morphogenesis and Cancer in 3D. *Cell* **2007**, *130*, 601–610.

(98) Langhans, S. A. Three-Dimensional In Vitro Cell Culture Models in Drug Discovery and Drug Repositioning. *Front. Pharmacol.* **2018**, *9*, 6.

(99) Reed, J.; Reed, T. A. A Set of Constructed Type Spectra for the Practical Estimation of Peptide Secondary Structure from Circular Dichroism. *Anal. Biochem.* **1997**, *254*, 36–40.

(100) Amon, M. A.; Ali, M.; Bender, V.; Hall, K.; Aguilar, M. I.; Aldrich-Wright, J.; Manolios, N. Kinetic and Conformational Properties of a Novel T-Cell Antigen Receptor Transmembrane Peptide in Model Membranes. *J. Pept. Sci.* **2008**, *14*, 714–724.

(101) Allen, M.; Poggiali, D.; Whitaker, K.; Marshall, T.; Kievit, R. Raincloud Plots: A Multi-Platform Tool for Robust Data Visualization [Version 1; Peer Review: 2 Approved]. *Wellcome Open Res.* **2019**, *4*, 63.

(102) Zar, J. H. In *Biostatistical Analysis*, 5th ed.; Zar, J. H., Ed.; Pearson Educations: Upper Saddle River, NJ, 2009.

(103) R Core Team. The R Project for Statistical Computing. https://www.r-project.org/ (accessed Feb 13, 2021).

(104) Pohlert, T. The Pairwise Multiple Comparison of Mean Ranks Package (Pmcmr). https://cran.r-project.org/web/packages/PMCMR/vignettes/PMCMR.pdf (accessed Feb 13, 2021).